Flicr, a long noncoding RNA, modulates Foxp3 expression and autoimmunity

David Zemmour[a], Alvin Pratama[a], Scott M. Loughhead[a], Diane Mathis[a,1], and Christophe Benoist[a,1]

[a]Division of Immunology, Department of Microbiology and Immunobiology, Harvard Medical School, Boston, MA 02115

Contributed by Christophe Benoist, March 8, 2017 (sent for review January 19, 2017; reviewed by Katherine A. Fitzgerald and Alexander Y. Rudensky)

A combination of transcription factors, enhancers, and epigenetic marks determines the expression of the key transcription factor FoxP3 in regulatory T cells (Tregs). Adding an additional layer of complexity, the long noncoding RNA (lncRNA) *Flicr* (*Foxp3* long intergenic noncoding RNA) is a negative regulator that tunes *Foxp3* expression, resulting in a subset of Tregs with twofold- to fivefold-lower levels of FoxP3 protein. The impact of *Flicr* is particularly marked in conditions of IL-2 deficiency, and, conversely, IL-2 represses *Flicr* expression. *Flicr* neighbors *Foxp3* in mouse and human genomes, is specifically expressed in mature Tregs, and acts only in *cis*. It does not affect DNA methylation, but modifies chromatin accessibility in the conserved noncoding sequence 3 (CNS3)/Accessible region 5 (AR5) region of *Foxp3*. Like many lncRNAs, *Flicr*'s molecular effects are subtle, but by curtailing Treg activity, *Flicr* markedly promotes autoimmune diabetes and, conversely, restrains antiviral responses. This mechanism of FoxP3 control may allow escape from dominant Treg control during infection or cancer, at the cost of heightened autoimmunity.

autoimmunity | regulatory T cells | gene regulation | long noncoding RNA | Foxp3

Regulatory T cells (Tregs), a subset of $CD4^+$ T cells determined by the transcription factor (TF) FoxP3, are fundamental actors in maintaining immune homeostasis, by dampening activation of several immunocyte lineages (1, 2). In their absence, humans and mice develop devastating autoimmune and lymphoproliferative pathologies (3). Although beneficial in preventing runaway immune activation, supporting tolerance of symbiotic microbes, and restraining tissue destruction in autoimmune lesions, their regulatory activity can also be deleterious, for example, by inhibiting antitumor (4) or antiviral responses (2, 5).

Phenotypic stability is important for Tregs (1, 6–8), particularly as their antigen receptors tend to show reactivity to self-antigens. This stability, and the stability of *Foxp3* expression, result from a combination of factors (9): DNA hypomethylation at conserved enhancer elements of *Foxp3* and other key loci (10) or self-reinforcing TF networks (11). This stability is bolstered by signals from IL-2, the key trophic cytokine for Tregs (2, 7, 9, 12, 13). At the center of this network lies FoxP3, the lineage-defining TF that is essential for Treg differentiation, maintenance, and function (1, 14–17). Several enhancer elements, conserved across vertebrates, ensure correct *Foxp3* expression, one of them [conserved noncoding sequence 2 (CNS2)] being important for the stability of *Foxp3* expression (18–20) during cell division and in proinflammatory milieus.

Deep transcriptome analyses have revealed the existence of an abundant class of long noncoding RNAs (lncRNAs) (21–24). LncRNAs do not encode proteins and are longer (>200 bp) than other noncoding transcripts like microRNAs. This family represents up to 20% of mammalian transcriptomes, which also applies in Tregs (25), and their expression is more tissue-specific than that of proteins. Evolving rapidly, they are poorly conserved evolutionarily, and only ∼10% of human lncRNAs have a clear homolog in mice (26). lncRNAs seem to be mostly involved in regulating gene expression through several mechanisms, which are conditioned by expression levels (typically low), subcellular localization (nuclear or cytoplasmic) and position in the genome (23). Some nuclear lncRNAs act in *cis* and activate or repress genes in their immediate vicinity; others have longer-range *cis* (e.g., *Xist* inactivates the entire X chromosome) (27) or *trans* action (*Hotair* and *Hox* genes) (28–30). Cytoplasmic lncRNAs also can interfere with translation, have catalytic activity, or act as miRNA sponges (31). In general, lncRNAs are thought to be modulators of expression patterns dictated by transcription regulators, although in some instances they have a dominant impact, as in the allelic inactivation of one copy of the X chromosome driven by *Xist*.

Relatively few lncRNAs specific to the immune system have been studied in detail in vivo, and their cumulative impact on immune functions remains largely unknown (32). Some lncRNAs are dynamically expressed during development (33), and others are important for granulocyte homeostasis (e.g., *Morrbid* regulates myeloid cell lifespan) (34) or immune effector functions (e.g., *Rmrp* and Th17 cell function, *NeST* and IFNγ expression in T cells) (35, 36). Consequently, lncRNAs influence the immunopathology of infections (*NeST*, *Morrbid*), endotoxic shock (*lincRNA-EPS*) (37), or gut inflammatory diseases (*Rmrp*, *linc-13*) (36, 38).

While analyzing lncRNA expression in Treg profiling data, we noticed the transcript *4930524L23Rik*. Its Treg-specific expression and genomic localization, partially overlapping *Foxp3*, were too striking to ignore. Here we report the structure, expression, and function of this lncRNA, hereinafter called *Flicr* (*Foxp3* long intergenic noncoding RNA). This lncRNA is present across mammalian species with clear stretches of sequence conservation. *Flicr* modulates *Foxp3* expression, most visibly in a subset of Tregs. This subtle fine-tuning has important consequences for autoimmune disease, thus subtly modulating the Janus-faced dominant suppressive function of Tregs.

Significance

Regulatory T cells (Tregs) are an essential population of immunoregulatory cells that play a central role in immune tolerance and the control of autoimmune disease, infections, and cancer. The transcription factor FoxP3 is the central orchestrator of Treg differentiation, stability, and function. Here we report the discovery of the noncoding RNA, *Flicr*, and its fine-tuning of FoxP3 expression through modification of chromatin accessibility, with marked consequences on the progression of autoimmune diabetes. Our findings add an important piece to the puzzle of Treg differentiation and stability, and how their function adapts to physiological circumstances.

Author contributions: D.Z., D.M., and C.B. designed research; D.Z., A.P., and S.M.L. performed research; D.Z. and C.B. analyzed data; and D.Z., D.M., and C.B. wrote the paper.

Reviewers: K.A.F., University of Massachusetts Medical School; and A.Y.R., Memorial Sloan-Kettering Cancer Center.

Conflict of interest statement: C.B. and Alexander Rudensky were coauthors on a 2013 publication. This was a nomenclature paper and did not involve any research collaboration.

Data deposition: The data reported in this paper have been deposited in the Gene Expression Omnibus (GEO) database, https://www.ncbi.nlm.nih.gov/geo (accession nos. GSE97048 and GSE97085).

[1]To whom correspondence should be addressed. Email: cbdm@hms.harvard.edu.

This article contains supporting information online at www.pnas.org/lookup/suppl/doi:10.1073/pnas.1700946114/-/DCSupplemental.

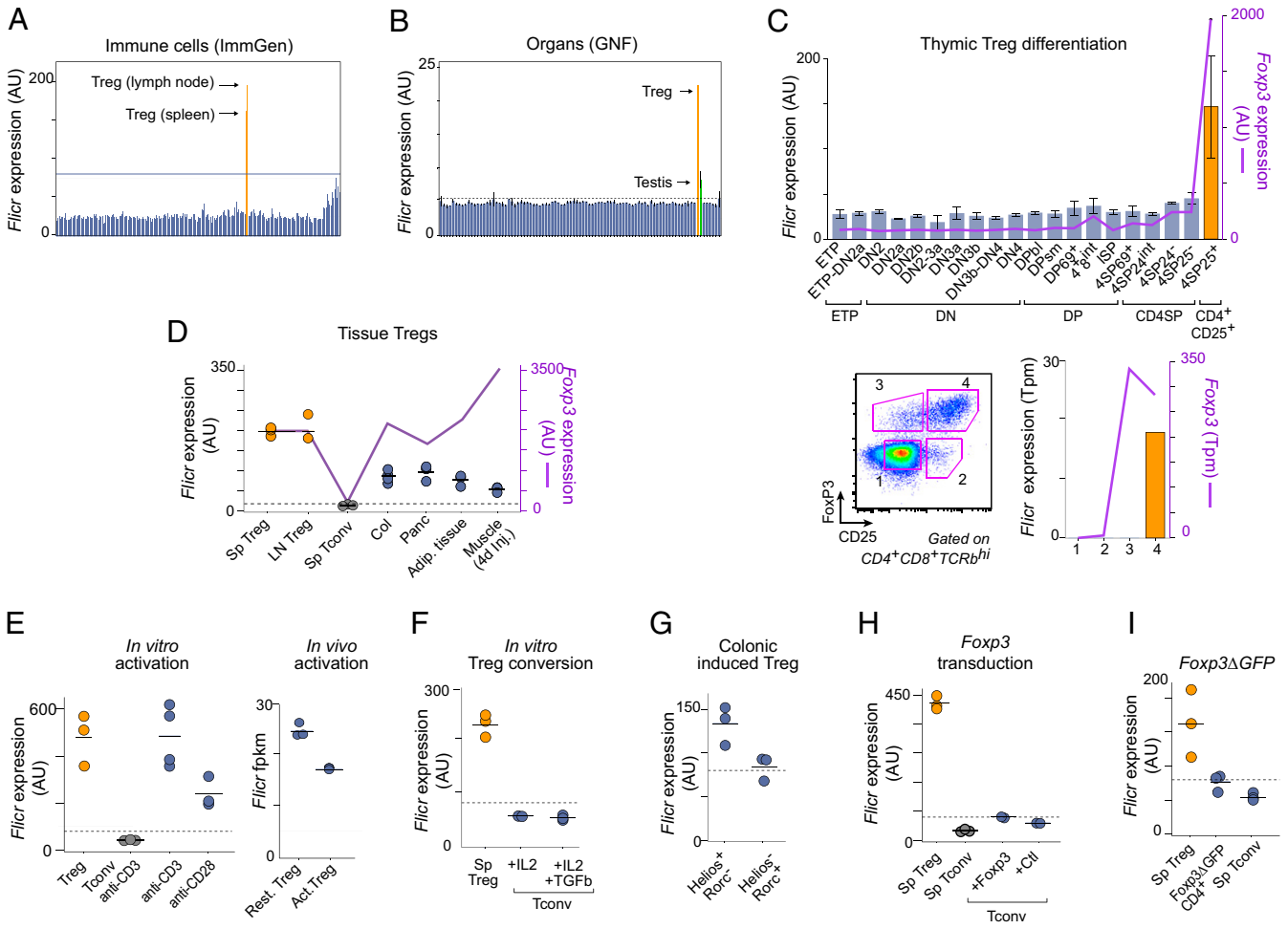

Fig. 1. *Flicr* is expressed specifically in Tregs. *Flicr* expression in various contexts. (*A* and *B*) ImmGen mouse immunocyte (39) or GNF mouse organ microarray compendia (40) (dashed lines: background level). (*C*) During thymic Treg differentiation. (*Left*) ImmGen data. (*Right*) RNA-Seq analysis of $CD4^+$ SP thymocytes sorted as shown; *y*-axis, transcripts per million (tpm). (*D*) Tissue Tregs. Each point is an individual mouse. Sp, spleen; Col, colonic lamina propria; Panc, pancreas; Adip. tissue, visceral adipose tissue; Muscle, injured muscle at 4 d postcardiotoxin injection. (*E*) After activation in vitro with anti-CD3/CD28 beads (42) (*Left*) or in vivo (41) (*Right*). Rest., resting $CD44^{lo}CD62L^{hi}$; Act., activated $CD44^{hi}CD62L^{lo}$ Tregs; rpkm, reads per kb per million reads. (*F*) In vitro converted induced Tregs (TCR activation with IL-2 and TGF-β) (43). (*G*) Ex vivo $Helios^-ROR\gamma^+$ colonic peripheral Tregs (44). (*H*) In Tconvs transduced with *Foxp3* or control retrovectors (11). (*I*) In Treg-like cells of mice with *Foxp3* inactivation by *Gfp* insertion (*Foxp3*Δ*Gfp*) (45).

Results

***Flicr*, an lncRNA Specifically Expressed in Tregs.** *Flicr* first caught our attention as an lncRNA detected only in Tregs among the ImmGen compendium of immunocyte gene expression (39) (Fig. 1*A*). This exclusivity was confirmed by RNA sequencing (RNA-Seq) analysis (Fig. S1). Outside of the immune system, *Flicr* was observed only in the testis, at low levels (40) (Fig. 1*B*). During Treg differentiation, it appeared concomitantly with *Foxp3* but only in the final $CD25^{hi}$ stage (Fig. 1*C*). *Flicr* was present in Tregs from all peripheral lymphoid organs and at lower levels in the specific Treg populations found in several nonlymphoid tissues (Fig. 1*D*). Tissue Tregs tend to have activated phenotypes and, accordingly, Treg activation slightly reduced *Flicr* expression in vivo (41) and in vitro (42) (Fig. 1*E*). In contrast, *Flicr* was not expressed in induced Tregs generated in vitro from naïve conventional T cells (Tconvs) with TGF-β and IL-2 (43) (Fig. 1*F*). That *Flicr* expression may require thymic Treg differentiation was consistent with its lower abundance in colonic $ROR\gamma^+$ $Helios^-$ Tregs, considered to result from extrathymic differentiation, relative to their thymically derived $ROR\gamma^-$ $Helios^+$ counterparts (44) (Fig. 1*G*). In keeping with the notion that FoxP3 alone is not sufficient to promote *Flicr* expression, transduction of *Foxp3* in $CD4^+$ T cells did not induce *Flicr* (11) (Fig. 1*H*). However, FoxP3 was necessary for *Flicr* expression, because Treg-like cells, in which *Foxp3* is transcriptionally active but encodes a nonfunctional protein, were *Flicr*-negative (45) (Fig. 1*I*).

Structure and Conservation of the Mouse and Human *FLICR*. We combined several types of analyses and external data sources to accurately position *Flicr* transcripts in the mouse genome (Fig. 2*A*), identifying four different isoforms of varying lengths (566, 737, 3,278, and 4,150 bp) that share two exonic elements and an intron, located 1.8 kb upstream of the *Foxp3* transcriptional start site (TSS). They are all transcribed from the same sense strand of *Chr*X as *Foxp3*, and the two longest ones overlap the *Foxp3* TSS. A 5′ rapid amplification of cDNA ends (RACE) analysis mapped several closely spaced 5′ ends of *Flicr* transcripts, concordant with CAGE data from the FANTOM Consortium (46) (Fig. S2*A*). However, we could not find evidence in Tregs for transcripts initiating further upstream and corresponding to the *4930524L23Rik* or *Ppp1r3fos* expressed sequence tags (ESTs) previously isolated from testis and thymus. A combination of 3′ RACE and polyA-tagged RNA-Seq data identified three main polyadenylation sites (Fig. 2*A* and Fig. S2*A*). These transcripts contained no open reading-frame (ORF) longer than 143 aa, and

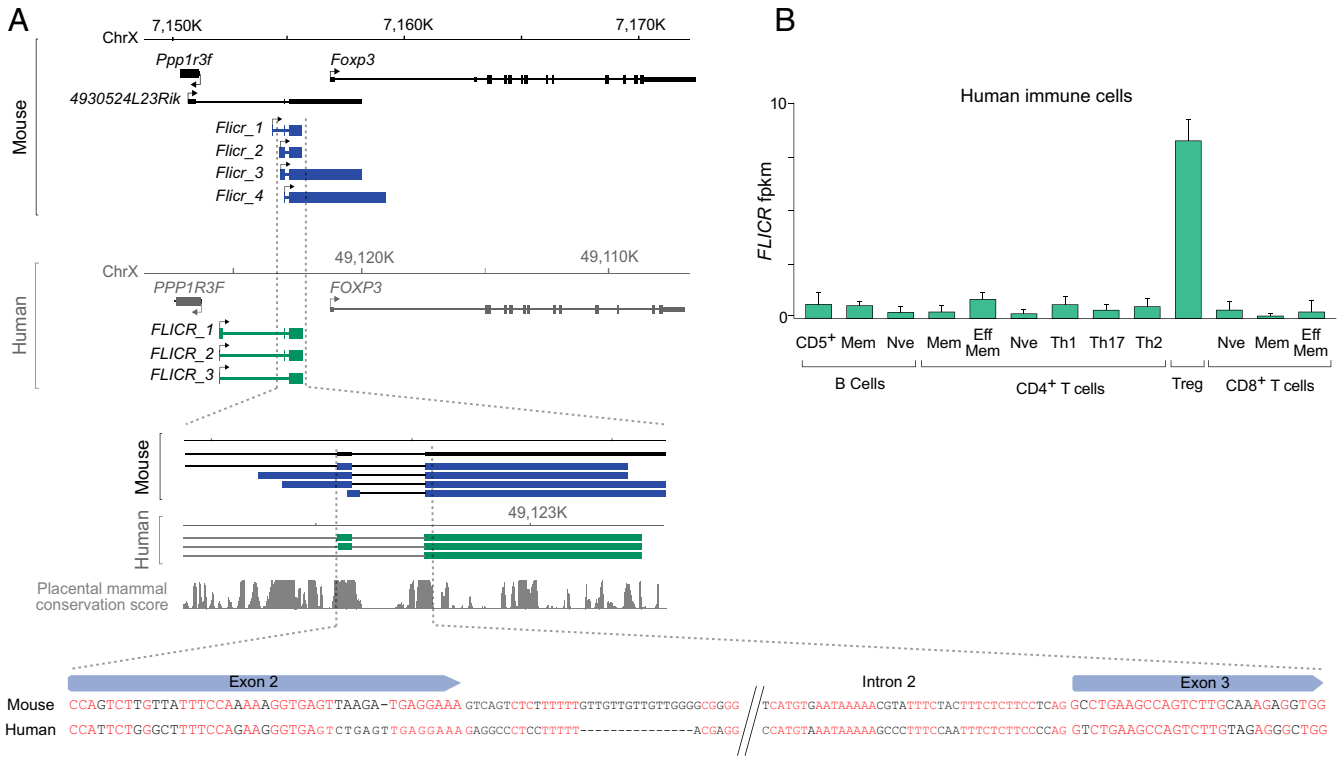

Fig. 2. *Flicr* is a conserved long noncoding RNA expressed in human Tregs. (*A*) Map of *Flicr* in the mouse (blue) and human (green) *FOXP3* loci (mm9 and hg19 coordinates), as deduced from the evidence shown in Fig. S2, shown at different levels of resolution, with PhastCons (69) placental mammal sequence conservation score. (*B*) *FLICR* expression by RNA-Seq in human lymphocyte populations (48). fpkm, fragments per kilobase per million.

had computationally predicted low peptide coding potential by codon substitution frequency analysis (PhyloCSF) (47); however, as for most lncRNAs, the possibility of translation into very short peptides cannot be ruled out (Fig. S2*C*).

lncRNAs are usually poorly conserved, but the region common to mouse *Flicr* isoforms showed distinct sequence homology to a similar location upstream of human *FOXP3* (Fig. 2*A*) and more generally among placental mammals. Indeed, focused PCR identified three *FLICR* isoforms in the human FOXP3$^+$ C5/MJ cell line, structures that were confirmed by parsing RNA-Seq from human Tregs (48). The main 5′ ends mapped closer to *PPP1R3F* than in the mouse, and we did not find *FLICR* transcripts that overlapped the *FOXP3* TSS, but the intron and flanking exons were again found ∼2 kb upstream of *FOXP3* (Fig. 2*A* and Fig. S2*B*). There was no preservation of putative ORFs in the conserved region, with nonsense or frame shift mutations in all possible reading frames (Fig. S2*C*). As in the mouse, *FLICR* expression was restricted to Tregs (Fig. 2*B*; human RNA-Seq) (48). Thus, human and mouse Tregs specifically express an lncRNA of very similar structure and position, situated very close to the *Foxp3* locus.

***Flicr* Dampens FoxP3 Expression in Tregs.** To determine its function, we generated a *Flicr*-deficient mouse line by deleting a short segment (263 bp) encompassing exon 2 and the splice junction, the focal point of sequence conservation (Fig. 3*A*), using CRISPR/Cas9 (clustered regularly interspaced short palindromic repeats) to introduce two specific breaks for nonhomologous end-joining in fertilized mouse eggs (49). We purposely kept the deletion very short to avoid affecting *Foxp3* enhancer elements, targeting a region devoid of H3K27Ac enhancer, H3K27me3 repressive marks, or CpG islands (Fig. S3*A*) (50). Indeed, transcriptome analysis showed that Tregs in *Flicr*-deficient (KO) mice lost *Flicr*, but not *Ppp1r3f* and *Foxp3* transcripts, the latter being slightly increased (Fig. 3*B*). KO mice developed and grew normally, with no histological evidence of systemic autoimmune disease. Treg differentiation and homeostasis seemed unchanged, with normal Treg proportions in the thymus, spleen, and lymph nodes (Fig. S3*B*); however, close examination of cytometry profiles revealed a consistent trait (Fig. 3*C*): whereas CD25^{hi} Tregs from WT mice showed the usual range of FoxP3 expression, with some cells having twofold to fivefold less FoxP3 than the main peak, *Flicr*-deficient Tregs had a tighter distribution, with significantly fewer FoxP3^{lo} Tregs. Correspondingly, the overall mean fluorescence intensity (MFI) increased slightly (Fig. 3*D*). This disappearance of the FoxP3^{lo} Tregs was observed in *Flicr*-deficient mice on the NOD background, where the mutation was initially constructed, and on the autoimmune-resistant B6xNOD background (Fig. S3*C*).

Although the *Flicr* KO deletion was relatively small (263 bp) and eschewed regulatory regions identifiable by chromatin marks, we wanted to assess definitively whether these observations could be explained by the deletion of a putative regulatory DNA element. First, the same reduction of FoxP3^{lo} cells was present in an independent *Flicr* mutant mouse in which only 12 bp at the splice junction of exon 3 were deleted (Fig. 3*A* and Fig. S3*D*). Unfortunately, only one progeny could be obtained from this line, precluding statistical analysis and follow-up, but nevertheless this provides confirmatory evidence. Second, we confirmed the results by an independent RNAi approach, transfecting locked nucleic acid (LNA) antisense oligonucleotide to target *Flicr* in Tregs in culture (34). Here again, a reduction in FoxP3^{lo} cells was observed (Fig. 3*E*), confirming a direct role of *Flicr* RNA on FoxP3 expression. Third, if *Flicr* down-regulates FoxP3 in a subset of cells, then it would be predicted to be overrepresented in FoxP3^{lo} cells. Indeed, more *Flicr* RNA was detected in cells with lower FoxP3 (Fig. 3*F*).

To test whether the FoxP3 phenotype of *Flicr*-deficient mice was Treg-autonomous or resulted from an indirect effect, we

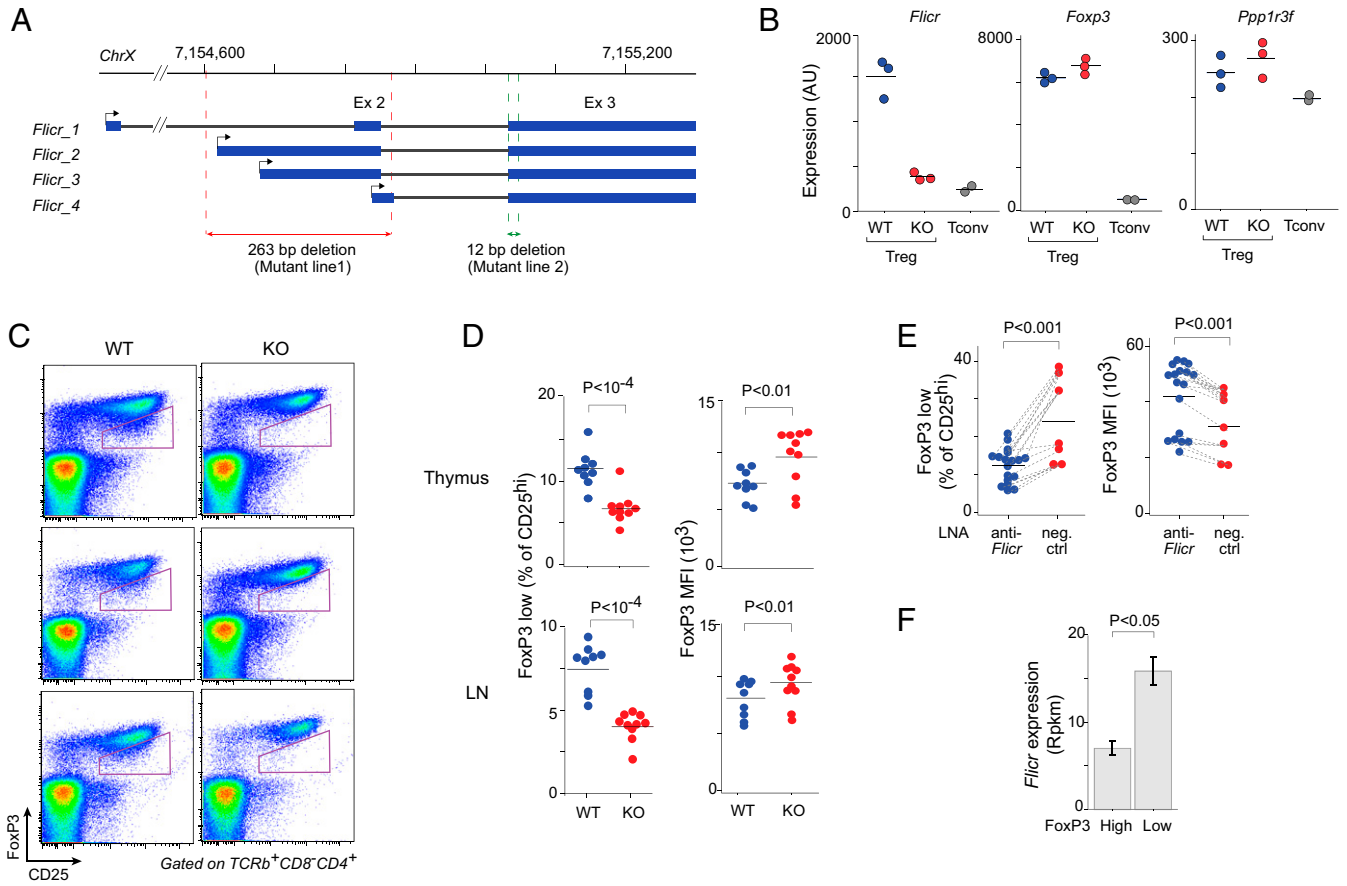

Fig. 3. *Flicr* KO and its action on FoxP3 expression. (*A*) Position of the 263-bp deletion of *Flicr* exon 2 (red) and of the second independent 12-bp deletion of the donor spliced site of exon 3 (green). (*B*) *Flicr*, *Foxp3*, and *Ppp1r3f* expression in *Flicr* WT and KO splenic Tregs and Tconvs (microarray, using only values from array probes mapping outside the deletion). (*C*) FoxP3 vs. CD25 expression in gated splenic $CD4^+$ T cells from in WT and KO mice. Representative plots from four experiments are shown. (*D*) FoxP3 MFI and proportion of $FoxP3^{lo}$ cells (per gating at left) in thymic and lymphoid $CD4^+$ T cells from in WT and KO mice, compiled from four experiments. (*E*) RNAi. FoxP3 MFI and proportion of $FoxP3^{lo}$ cells in activated $CD4^+$ T cells transfected with anti-*Flicr* or control LNAs. Data are compiled from three experiments, one of which had lower staining intensity for technical reasons. (*F*) *Flicr* expression in $FoxP3^{high}$ and $FoxP3^{low}$ in RNA-Seq data (19). *P* values from ANOVA (*D* and *E*) or *t* test (*F*).

constructed mixed chimeras. Alymphoid *Rag*-deficient hosts were reconstituted with equal proportions of bone marrow from *Flicr* WT and KO donors. In this setting, we again observed the "tightening" of FoxP3 expression in Tregs of *Flicr* KO genotype, relative to WT Tregs in the same hosts (Fig. 4*A*), indicating a Treg-intrinsic effect. Interestingly, KO Tregs had a competitive advantage over their WT counterparts in the same mice; the ratio of cells of KO vs. WT origin was consistently higher in Tregs than in $CD4^+$ Tconvs in the same mice (Fig. 4*B*, *Left*), which resulted in a higher proportion of Tregs in the KO pool (Fig. 4*B*), revealing better fitness of *Flicr*-deficient Tregs than was observed in the full KO mice.

***Flicr* Destabilizes FoxP3 Expression in Conditions of Limiting IL-2.** The foregoing results suggested that *Flicr* affects the stability of FoxP3 expression in some Tregs. For confirmation, we cultured Tregs in conditions of limited IL-2, under which FoxP3 tends to be lost (51). The $FoxP3^{lo}$ cells that normally appear in low–IL-2 cultures were essentially absent in Treg cultures from *Flicr*-deficient mice (Fig. 5*A*). Thus, the subtle effect observed under steady state was magnified when trophic support became limiting.

These results also suggested that IL-2 and *Flicr* are diametric opposites with regard to Treg homeostasis. Because IL-2 signaling stabilizes FoxP3 expression by recruiting the transcription factor STAT5b to the *Foxp3* locus (52), we hypothesized that it might inhibit *Flicr* to maintain *Foxp3* expression. Indeed, provision of IL-2 lowered *Flicr* expression in culture (Fig. 5*B*). Interestingly, a slight accumulation of STAT5b was present in the *FLICR* promoter region in a ChIP sequencing analysis of human Tregs (53) (Fig. 5*C*), suggesting a pathway by which IL-2 might repress *Flicr* directly. Thus, *Flicr* appeared to be an active mechanism of *Foxp3* destabilization, which IL-2 counteracts.

***Flicr* Acts only in *Cis*.** PCR quantitation after nuclear-cytoplasmic fractionation showed that *Flicr*, like *Xist*, resides primarily in the nucleus (Fig. S4*A*), suggesting that it might regulate transcription. We asked whether *Flicr* had broader effects in Tregs beyond its *cis* action on the neighboring *Foxp3* gene. A comparison of *Flicr* WT and KO Tregs showed a very limited impact on gene expression profiles (from no changes to a twofold increase; Fig. 6*A*). Signature genes overexpressed in Tregs were biased toward underexpression in WT cells ($P = 2 \times 10^{-5}$), and the transcripts most affected by the deletion of *Flicr* were Treg signature genes (Fig. 6*B*). Similarly, FoxP3-binding genomic targets (ChIP sequencing data from ref. 54) were mostly underexpressed in WT Tregs compared with KO Tregs (Fig. 6*C*). These findings suggest that many/most of *Flicr*'s effects result from lowering or destabilization of *Foxp3* expression.

Given its position, *Flicr* seemed likely to influence *Foxp3* transcription through a local *cis* effect, as is the case for several

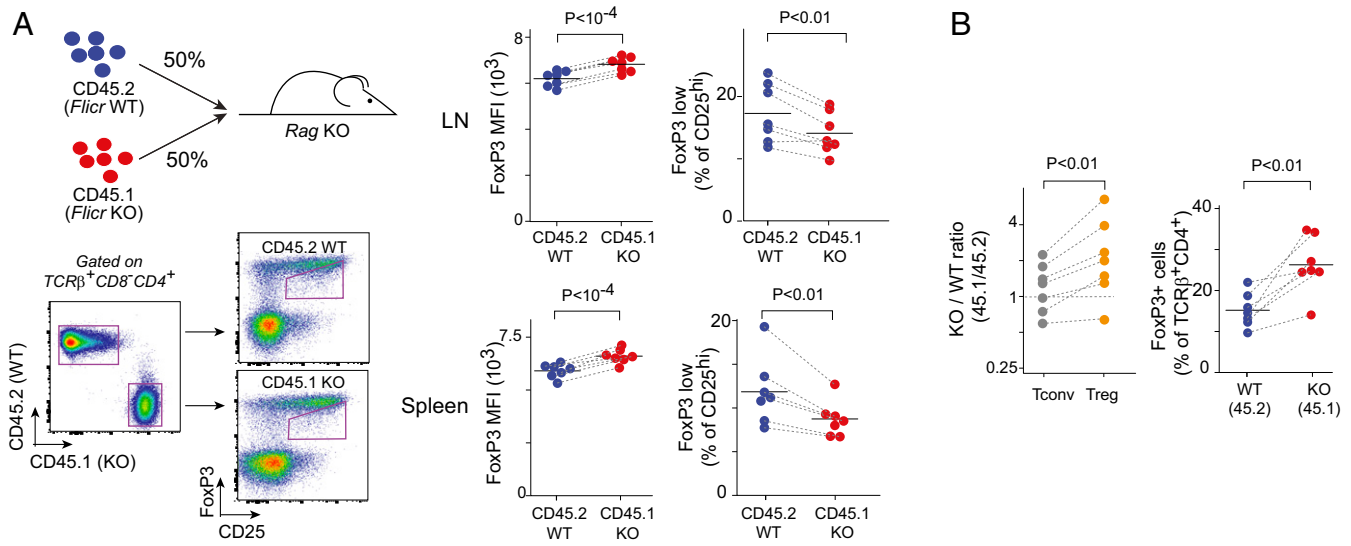

Fig. 4. Cell-intrinsic effect of *Flicr* on FoxP3 expression. (*A*) *Rag*-KO mice were reconstituted with equal proportions of congenically labeled bone marrow cells from *Flicr* WT (CD45.2) and KO (CD45.1) mice. Shown are representative FACS plots distinguishing CD4$^+$ T cells of different origins for FoxP3 vs. CD25 analysis (*Left*), FoxP3 MFI (*Middle*), and proportion of FoxP3^{lo} cells (*Right*) in Tregs in KO and WT compartments in the same mice. (*B*, *Left*) Relative proportions of *Flicr* KO- vs. *Flicr* WT-derived Treg and Tconv splenocytes in the same mice. (*B*, *Right*) Splenic proportions of Tregs in the WT and KO compartments. All *P* values are from the paired Student *t* test.

lncRNAs (27, 30, 55). We tested this hypothesis by attempting to complement *Flicr* KO mice with a BAC transgene that includes a WT *Flicr*, together with an insertionally inactivated *Foxp3* (56) (Fig. 6*D*). Although the transgene-encoded *Flicr* was expressed at the same level as the endogenous one (Fig. S4*B*), it did not restore FoxP3^{lo} Tregs in vivo (Fig. 6*E*) or the sensitivity to low IL-2 supply in vitro (Fig. 6*F*). Expression of the genes affected by the *Flicr* deficiency also was not normalized by the *Flicr*-encoding complementing transgene (Fig. S4*B*), reinforcing the notion that *Flicr*'s influence on their expression is indirect, via FoxP3. Thus, *Flicr's* genomic proximity to *Foxp3* is necessary for its mechanism of action. These results show that *Flicr* is a nuclear lncRNA that acts in *cis* on *Foxp3* expression, and indirectly has a subtle but broader impact on the Treg transcriptome.

***Flicr* Influences Focal Chromatin Accessibility in the Foxp3 Locus.** Given that *Flicr* acts in *cis*, we reasoned that it might influence the *Foxp3* epigenetic landscape. Methylation at several CpG clusters

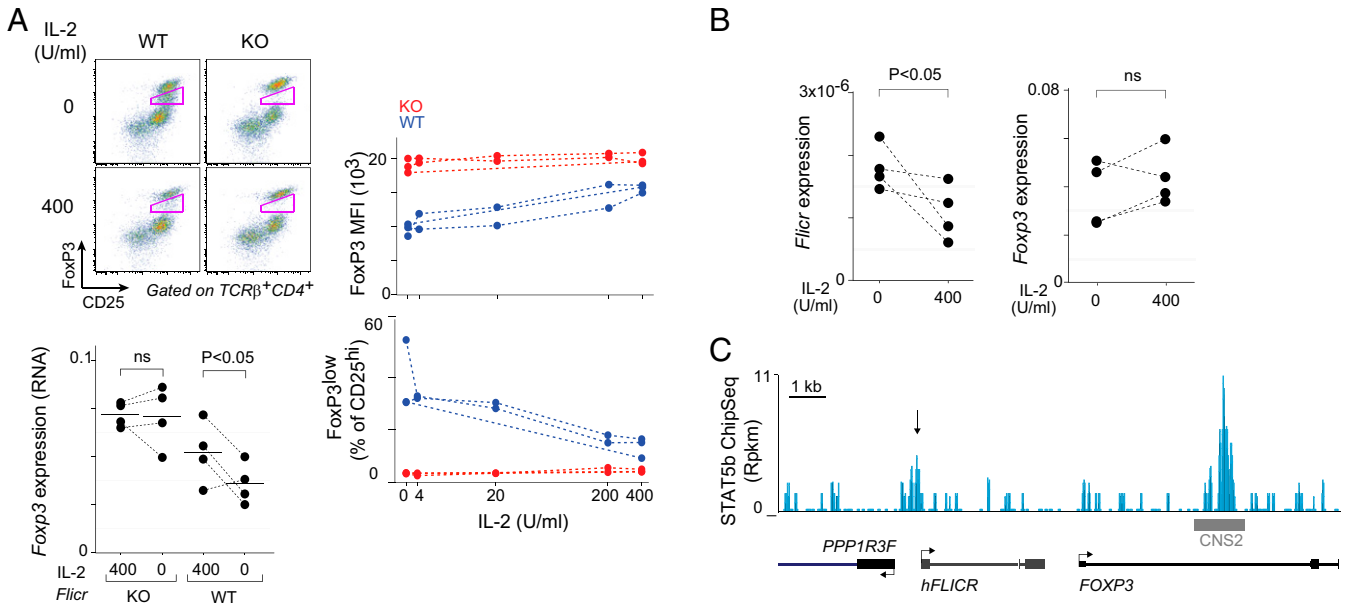

Fig. 5. *Flicr* destabilizes FoxP3 expression in vitro and is down-regulated by IL-2. (*A*) In vitro stability assay. Tregs were cultured for 48 h in limiting IL-2 before cytometry. (*Left*) Representative FoxP3 vs. CD25 plot. (*Middle*) FoxP3 MFI and proportion of FoxP3^{lo} cells. (*Right*) *Foxp3* expression (relative to *Acting1*) by RT-qPCR. Data are pooled from three experiments. (*B*) *Flicr* and *Foxp3* expression (relative to *Acting1*) by RT-qPCR in purified Tregs after 2 h in culture with or without IL-2. Data are pooled from two experiments. *P* values are from ANOVA. (*C*) STAT5b binding to the *FLICR* promoter and the CNS2 enhancer in chromatin immunoprecipitation (53).

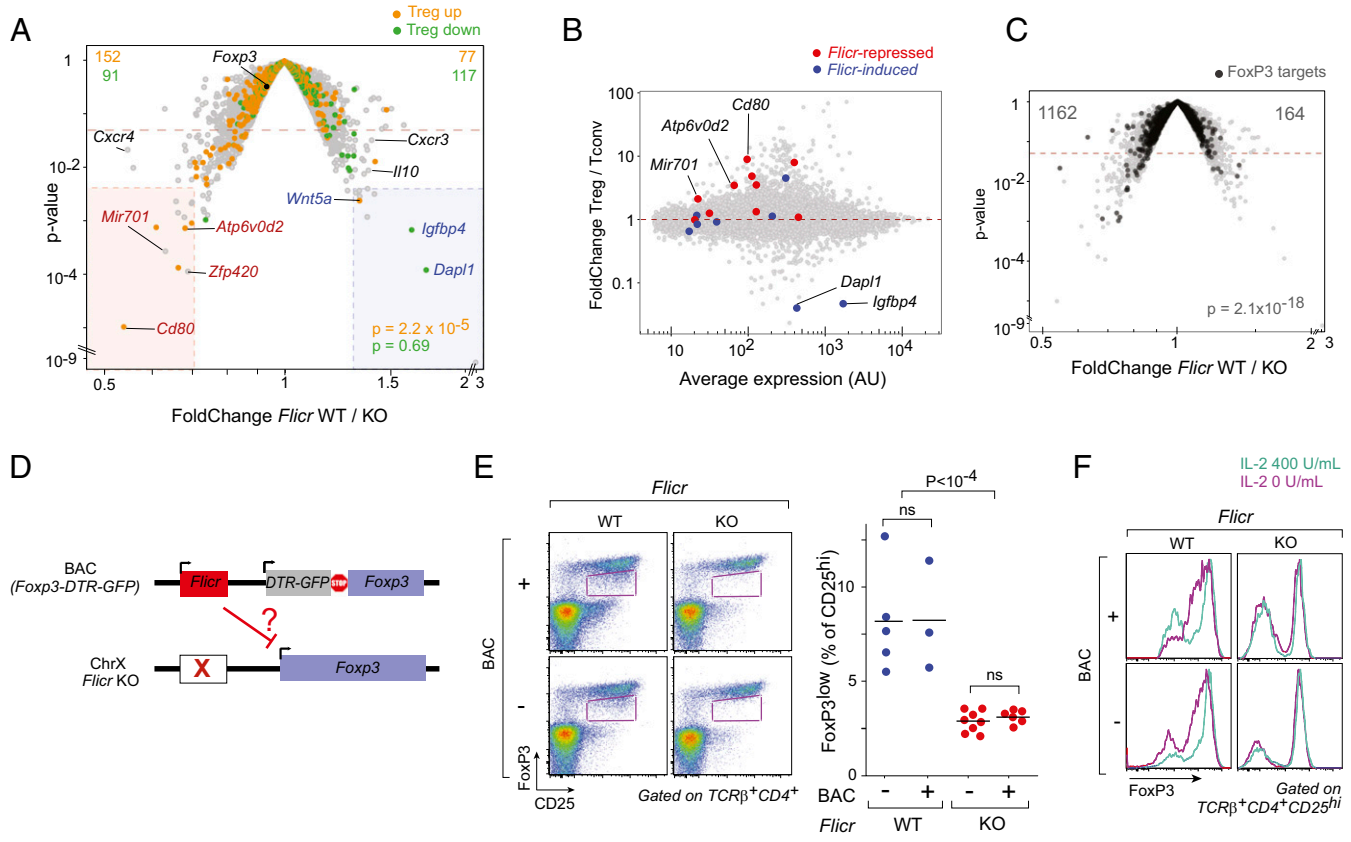

Fig. 6. Impact of *Flicr* on FoxP3 regulated genes. (*A*) Comparison of gene expression profiles of *Flicr*-WT and -KO Tregs (microarray). Up- and down-regulated Treg signature genes (70) are highlighted. *P* values are from the χ^2 test. (*B*) Expression/fold change plot of normal Treg vs. Tconv profiles (70) highlighted with transcripts up- or down-expressed in WT vs. KO (as gated in *A*). (*C*) Same volcano plot as in *A*, with black highlights indicating genes that bind FoxP3 in Treg chromatin (54). (*D*) Complementation experiment design. *Flicr* KO mice were crossed with mice carrying a BAC transgene encompassing WT *Flicr* and an insertionally inactivated *Foxp3* (56), tested for a *trans* effect on endogenous *Foxp3*. (*E*) FoxP3 protein expression in $CD4^+$ splenocytes from *Flicr* WT and KO mice, with or without genetic complementation by the *Flicr* BAC transgene. Shown are representative plots and results compiled from five experiments. *P* values are from ANOVA. (*F*) In vitro stability assay, as shown in Fig. 4*A*, in Tregs from the same mice as in *E*. A representative plot of five experiments is shown.

within the *Foxp3* locus, particularly in the CNS2 enhancer region, correlates with the stability of its expression (10, 57). However, comparison of methylation at the *Foxp3* locus in *Flicr* WT and KO Tregs showed superimposable profiles, except for a minor alteration within *Flicr* itself (Fig. 7*A*). Treg-specific hypomethylation at CNS2 was intact.

We then used assay for transposase-accessible chromatin (ATAC) high-throughput sequencing (ATAC-seq), which probes chromatin openness by its accessibility to the Tn5 transposase, and produces detailed information on the configuration of hypersensitive TSS and enhancer elements (58). Six accessible regions were identifiable across *Foxp3* in Tregs: the promoter, the CNS2 and CNS3 enhancers (20), two other regions [hereinafter referred to as accessible regions (AR) 5 and 6], and the 3′ UTR (Fig. 7*B*). Overall, ATAC-seq profiles were very similar in *Flicr* WT and KO Tregs, but close examination revealed reciprocal shifts at Accessible region 5 (AR5) [less accessible in KO Tregs; $P = 0.03$ based on the genome-wide variance distribution between replicates (DiffBind)] (Fig. 7*B*) and CNS3 (more accessible; $P = 0.01$). These shifts were reproducible in independent experiments, as was the increased accessibility in the 3′ UTR, possibly reflecting altered Pol-II recycling. In contrast, CNS2 profiles did not vary.

Physiological Consequences of *Flicr* Deletion. FoxP3 stability is needed to maintain Treg homeostasis and prevent autoimmunity (6). An active mechanism that destabilized *Foxp3* expression in Tregs might be advantageous as a "back door" to avoid dominant Treg control in some circumstances, but also seems risky. We tested immune function in *Flicr*-deficient mice in several Treg-dependent settings. A first set of experiments showed identical growth of the MC38 tumor line in *Flicr* WT and KO hosts. We then tested the notion that *Flicr* might promote autoimmunity by destabilizing Treg function (8, 56), and analyzed the course of autoimmune diabetes in *Flicr*-deficient NOD females. These mice showed a significantly reduced rate and incidence of overt diabetes (Fig. 8*A*). This halving of diabetes incidence was reflected in reduced severity of insulitis at age 11 wk (Fig. 8*B*). In the inflammatory context of these infiltrated islets (Fig. 8*C*), Tregs showed the same stabilization of FoxP3 levels in the absence of *Flicr* as they did in lymphoid organs. As reported previously (59), insulitis was inversely correlated with the proportion of Treg in the pancreas (Fig. 8*D*). Interestingly, the slope of this anticorrelation was steeper in *Flicr* KO mice than in heterozygous or WT control littermates ($r = -0.91$ vs. $r = -0.46$; $P = 0.05$), possibly suggesting that *Flicr*-deficient Tregs are functionally more efficient on a per-cell basis, reminiscent of the superior fitness noted above.

Discussion

Here we report the discovery of the lncRNA *Flicr*, a negative regulator of *Foxp3* expression in Tregs. It appears to act exclusively in *cis*, but by controlling FoxP3 has wider effects on the specific Treg transcriptome and Treg fitness. Its molecular effects are subtle, and more particularly visible in a subset of Tregs,

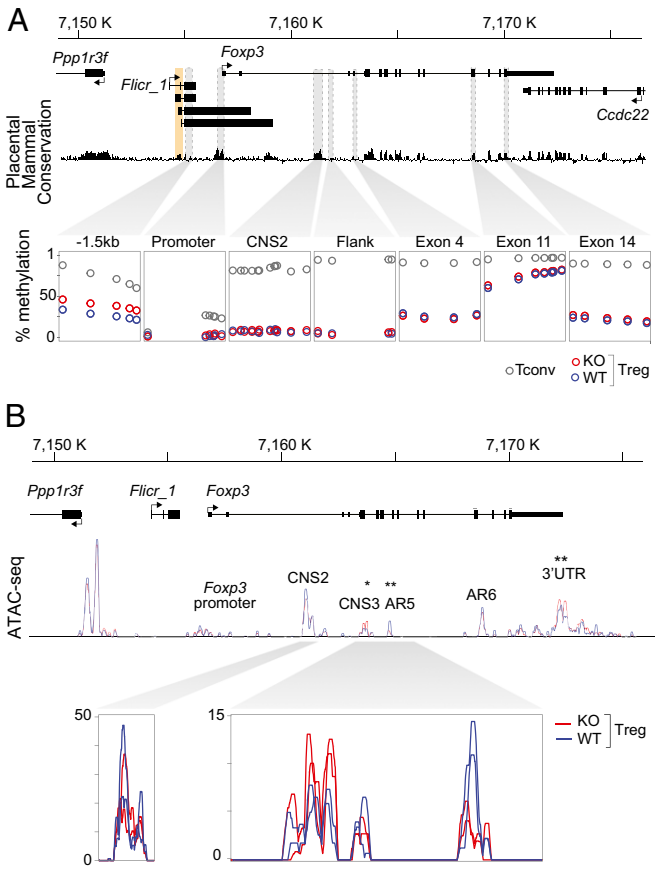

Fig. 7. *Cis* effect of *Flicr* on *Foxp3* chromatin accessibility. (*A*) CpG methylation profile of the *Foxp3* locus in *Flicr* WT and KO Tregs (bisulfite sequencing). Each dot represents one 5-methylcytosine site; methylation frequency is averaged from two independent experiments. (*B*) Chromatin accessibility (ATAC sequencing) at the *Foxp3* locus in WT and KO Tregs (red and blue lines, respectively). Two independent experiments are shown. $*P < 0.05$, $**P < 0.01$, differential peak analysis (Diffbind; negative binomial distribution).

but they have a marked impact on the efficacy of peripheral immunologic tolerance. The *Foxp3* locus appears to come directly equipped with a counterregulatory mechanism.

Based on its genomic location, expression pattern, and physiological impact, *Flicr* seems to be one of the lncRNAs that selectively modulates a specific physiological function, here Treg activity. FoxP3 does not merely obey on/off regulation to dictate Treg repressive functions, but can be tuned in response to different environmental cues, particularly in conditions of limiting IL-2 (2, 4, 18, 19). These results show that IL-2 has two means of enhancing *Foxp3* expression, directly via activation of the *Cns2* enhancer and indirectly by repressing *Flicr*, the attenuator of *Foxp3*. *Flicr* expression is also curtailed in conditions of heightened Treg activation and functionality, in tissue Tregs and after TCR activation. By destabilizing *Foxp3*, *Flicr* dampens the Treg signature and may lower Treg stability, allowing stronger antiviral responses but also increasing the risk of as autoimmune disease.

Like other lncRNAs in the immune system (60), *Flicr* has a focused role that matches its expression. In this respect, it contrasts with *Rmrp*, the impact of which in T lymphocytes seems limited to Th17 cells despite ubiquitous expression (36), but is akin in this respect to *Morrbid* (34) and *NeST* (35), which have a range of activity conditioned by their restricted expression. From the lack of *trans* complementation by the *Flicr*-expressing BAC transgene, we infer that the mild bias that it imparts on other loci, predominantly Treg signature genes, is indirectly due to FoxP3 dampening. Several of these Treg signature genes are related to the different mechanisms through which Treg cells exert their suppressive activity (61). Thus, modification of the stability of FoxP3 expression and shifts in Treg signature genes likely contribute to the down-modulation of Treg function and fitness by *Flicr*. Importantly, *Flicr* seems to preferentially impact a subset of Tregs; increased FoxP3 levels are seen not in the main Treg pool, in which mean FoxP3 levels are not noticeably affected, but rather in the FoxP3^{lo} subset. We speculate that in vivo FoxP3^{lo} Tregs are equivalent to those observed in vitro when IL-2 is limiting, and that *Flicr* may be hastening their shutdown of FoxP3 expression.

Cis-acting lncRNAs have several modes of action (30). The localized human/mouse sequence conservation suggests that it is not akin to lncRNAs, the very transcription of which is regulatory by promoter interference, but that the primary or secondary structure of the RNA matters (30), possibly involving the splicing machinery given that the sequence conservation extends into the intron. Like many other lncRNAs, *Flicr*'s molecular signature is subtle, but ultimately results in a larger shift in the outcome of pancreatic autoimmunity and the progression to overt diabetes. This amplification is congruent with the observation that many of the genetic variants (eQTLs) that condition the propensity to autoimmune disease have only subtle effects on the expression of the gene that they influence. Because much of lymphocyte differentiation is related to engagement by self molecules, the immune system is likely tuned at the edge of autoimmunity, and

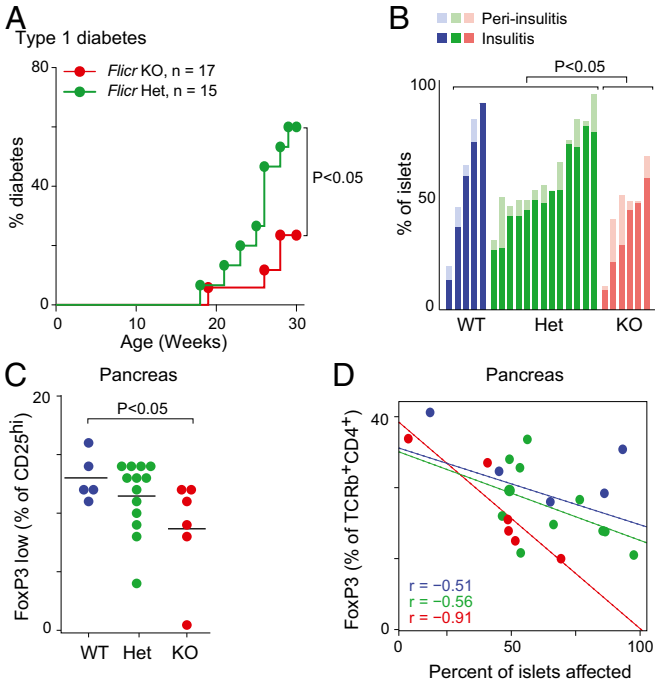

Fig. 8. Physiological consequences of modulation of Treg activity by *Flicr*. (*A*) Incidence of diabetes in *Flicr* KO and heterozygous littermate NOD females; *P* values from the Mantel–Cox log-rank test. (*B*) Proportion of infiltrated islets in the pancreas of 10-wk-old *Flicr* WT, heterozygous, and KO NOD females. *P* values are from the Mann–Whitney *U* test. (*C*) Proportion of FoxP3^{lo} in CD25^{hi} Tregs in the pancreas of 10-wk-old WT, heterozygous, and KO mice. Data are pooled from six experiments; Student *t* test. (*D*) Inverse correlation between islet infiltration and the proportions of Tregs among CD45^{+} cells in the pancreas. Lines represent linear regression fits for *Flicr* WT (blue), heterozygous (green), and KO (red). *P* values were obtained using Fisher *z*-transformation.

small changes, here in Treg fitness, can tip the system toward serious autoimmune consequences.

Different mechanisms are involved in controlling the stability of Foxp3 expression. At the epigenetic level, the CNS2 enhancer plays a critical role, reinforced by DNA methylation (10), and by integrating signals from the TCR and the IL-2 receptor (18, 19). However, *Flicr* does not seem to influence DNA methylation or chromatin accessibility at CNS2, but instead affects chromatin structure in the CNS3/AR5 region. CNS3 previously has been described as a poised enhancer open more generally in the T-cell lineage and important for Treg differentiation (41). Our results suggest this region also has a role in mature Tregs, balanced with AR5. lncRNAs commonly operate within ribonucleoprotein complexes with specific TFs (36), chromatin modifiers (28), or Hnrnp proteins (37, 60), and we propose that *Flicr* may target a repressive complex to the CNS3/AR5 region of *Foxp3*.

The functions of lncRNAs in the immune system are just being elucidated. Through its effects on Tregs, *FLICR* may be associated with human diseases associated with enhanced Treg activity, like infections or tumors, and its modulation opens avenues to suppress or enhance Treg function.

Materials and Methods

All experimental procedures are described in detail in *SI Materials and Methods*.

Mice. C57BL/6J mice were obtained from The Jackson Laboratory. NOD/Lt/DOI and Foxp3-DTR-GFP/N (56), Foxp3-Ires-Thy1.1/B6 (62), and Foxp3-IRES-GFP/B6 (63) mice were maintained in our colony. Foxp3-DTR-GFP/N carries a BAC transgene encompassing 150 kb downstream and 70 kb upstream of the *Foxp3* TSS, with a DTR-eGFP-stop insertion between the first and second codons of Foxp3. All experimentation was performed following animal protocol guidelines of Harvard Medical School (reviewed and approved HMS IACUC protocols 02954).

Mapping of Mouse and Human *Flicr* Transcripts. Treg RNA was prepared from double-sorted $CD4^+$ $TCR\beta^+$ $Thy1.1^+$ Tregs from Foxp3-Ires-Thy1.1/B6 mice. 3′ and 5′ RACE were performed using the SMARTer RACE cDNA Amplification Kit (Clontech), followed by Sanger sequencing. The 3′ termini were also mapped using RNA-Seq, and 5′ extremities were mapped from the FANTOM CAGE data (46). Exploratory PCR was performed using primers spanning the 4930524L23Rik locus, as shown in Fig. S2*A*. Isoforms were cloned with primers designed based on the extremities found. RNA from the $FOXP3^+$ C5/MJ HTLV1-transformed cells [American Type Culture Collection (ATCC); CRL-8293] was used to map human *FLICR* (3′ and 5′ RACE), and confirmed by Treg RNA-Seq data (48).

***Flicr* KO Mice.** To generate *Flicr*-deficient mice using the CRISPR/Cas9 system, we closely followed the method of Yang et al. (49) with several modifications. Because the active region of *Flicr* is unknown, we chose to introduce a point mutation using one guide RNA (gRNA) targeting the shared splice donor site or to delete a whole exon (exon 2) using two gRNAs, encompassing the region of highest homology between mouse and human transcripts, but keeping the mutation as small as possible to avoid interfering with *Foxp3* enhancer elements. Two mutants were obtained. One founder had a 12-bp deletion deleting the donor spliced site of exon 3, but gave only one progeny. Another mutant had a 263-bp deletion spanning *Flicr* exon 2.

In Vitro FoxP3 Stability. $CD4^+$ T cells from spleen and subcutaneous lymph nodes isolated by magnetic negative selection and $CD4^+TCR\beta^+CD25^{hi}$ (top 50%) Tregs were sorted by flow cytometry, then cultured with anti-CD3/CD28 beads (1:1 bead:cell; Gibco) and IL-2 (Peprotech; 212–12).

Gene Expression Profiling by Microarray. Microarray preparation and analysis were performed in accordance with ImmGen protocols (39). In brief, 50,000 $CD4^+TCR\beta^+CD25^{hi}$ (top 50%) Tregs and $CD25^-$ Tconvs isolated from pooled spleen and subcutaneous lymph nodes from 8-wk-old *Flicr* WT and KO mice were double-sorted as above. RNA was prepared from TRIzol extracts and used to prepare probes for Affymetrix Mouse Gene 1.0 ST arrays. Gene expression differences were calculated using the lmFit and eBayes functions of the limma package (64).

ATAC-seq. ATAC-seq was performed in biological duplicates following the protocol described by Buenrostro et al. (58). In brief, 50,000 $CD4^+TCR\beta^+CD25^{hi}$ (top 50%) Tregs were sorted and lysed. After transposition and PCR, final bead purification and selection (100–600 bp) were performed twice using 0.6× and 1.6× solid phase reversible immobilization (SPRI) beads. Libraries were paired-end sequenced (40, 50) using a 75-bp kit on an Illumina NextSeq High-Throughput Sequencing System.

Reads were filtered for quality and adapter-trimmed before mapping to the mm9 mouse genome. Reads mapping to multiple positions and PCR duplicates were discarded. Nucleosome free fragments (<120 bp) were analyzed, and peaks were called using Homer (65). Data were imported in R, and differential peak analysis was performed using DiffBind (differential peak analysis based on negative binomial distributions) (66).

Methylation Analysis by Bisulfite Treatment and High-Throughput Sequencing. The protocol was adapted from Feng et al. (18). Here 80,000 $CD25^{hi}$ Tregs were sorted as above, and DNA was purified and bisulfite-converted using the EZ DNA Methylation Direct Kit (Zymo Research), amplified by PCR. Illumina adapters were ligated and libraries amplified by a final PCR before sequencing using an Illumina MiSeq system. Reads were trimmed of the adapter aligned to the mm9 genome using Bismark (67). Data were analyzed and visualized using custom R scripts and the BiSeq library (68).

Autoimmune Diabetes. For diabetes incidence, mice were screened for diabetes by glucose urinalysis every week for 30 wk. A positive strip test was confirmed by blood analysis, and animals were considered diabetic with glucose >250 mg/dL on 2 consecutive days.

For histological evaluation, formalin-fixed and paraffin-embedded pancreas was sectioned and stained with hematoxylin and eosin. Four steps sections separated by 100 μm were used to calculate the insulitis score for each islet cells (0, no infiltration; 1, peri-insulitis; 2, intraislet insulitis), and 100 independent islets were scored for each mouse.

ACKNOWLEDGMENTS. We thank Drs. J. Rinn and J. Henao-Mejia for insightful discussions and materials, and L. Du, K. Hattori, A. Rhoads, C. Araneo, K. Waraska, M. Thorsen, and R. Steen for help with mouse profiling, sorting, and sequencing. This work was supported by NIH Grants AI051530 and AI116834 and the JPB Foundation. D.Z. was supported by a fellowship from the Boehringer Ingelheim Fonds.

1. Josefowicz SZ, Lu LF, Rudensky AY (2012) Regulatory T cells: Mechanisms of differentiation and function. *Annu Rev Immunol* 30:531–564.
2. Smigiel KS, Srivastava S, Stolley JM, Campbell DJ (2014) Regulatory T-cell homeostasis: Steady-state maintenance and modulation during inflammation. *Immunol Rev* 259: 40–59.
3. Bennett CL, et al. (2001) The immune dysregulation, polyendocrinopathy, enteropathy, X-linked syndrome (IPEX) is caused by mutations of FOXP3. *Nat Genet* 27:20–21.
4. Saito T, et al. (2016) Two FOXP3(+)CD4(+) T cell subpopulations distinctly control the prognosis of colorectal cancers. *Nat Med* 22:679–684.
5. Belkaid Y, Tarbell K (2009) Regulatory T cells in the control of host-microorganism interactions. *Annu Rev Immunol* 27:551–589.
6. Sawant DV, Vignali DA (2014) Once a Treg, always a Treg? *Immunol Rev* 259:173–191.
7. Rubtsov YP, et al. (2010) Stability of the regulatory T cell lineage in vivo. *Science* 329: 1667–1671.
8. Zhou X, et al. (2009) Instability of the transcription factor Foxp3 leads to the generation of pathogenic memory T cells in vivo. *Nat Immunol* 10:1000–1007.
9. Li X, Zheng Y (2015) Regulatory T cell identity: Formation and maintenance. *Trends Immunol* 36:344–353.
10. Floess S, et al. (2007) Epigenetic control of the foxp3 locus in regulatory T cells. *PLoS Biol* 5:e38.
11. Fu W, et al. (2012) A multiply redundant genetic switch "locks in" the transcriptional signature of regulatory T cells. *Nat Immunol* 13:972–980.
12. Fontenot JD, Rasmussen JP, Gavin MA, Rudensky AY (2005) A function for interleukin 2 in Foxp3-expressing regulatory T cells. *Nat Immunol* 6:1142–1151.
13. Setoguchi R, Hori S, Takahashi T, Sakaguchi S (2005) Homeostatic maintenance of natural Foxp3(+) CD25(+) CD4(+) regulatory T cells by interleukin (IL)-2 and induction of autoimmune disease by IL-2 neutralization. *J Exp Med* 201:723–735.
14. Fontenot JD, Gavin MA, Rudensky AY (2003) Foxp3 programs the development and function of $CD4^+CD25^+$ regulatory T cells. *Nat Immunol* 4:330–336.
15. Hori S, Nomura T, Sakaguchi S (2003) Control of regulatory T cell development by the transcription factor Foxp3. *Science* 299:1057–1061.
16. Hill JA, et al. (2007) Foxp3 transcription factor-dependent and -independent regulation of the regulatory T cell transcriptional signature. *Immunity* 27:786–800.
17. Williams LM, Rudensky AY (2007) Maintenance of the Foxp3-dependent developmental program in mature regulatory T cells requires continued expression of Foxp3. *Nat Immunol* 8:277–284.

18. Feng Y, et al. (2014) Control of the inheritance of regulatory T cell identity by a cis element in the Foxp3 locus. *Cell* 158:749–763.
19. Li X, Liang Y, LeBlanc M, Benner C, Zheng Y (2014) Function of a Foxp3 cis-element in protecting regulatory T cell identity. *Cell* 158:734–748.
20. Zheng Y, et al. (2010) Role of conserved non-coding DNA elements in the Foxp3 gene in regulatory T-cell fate. *Nature* 463:808–812.
21. Kapranov P, et al. (2002) Large-scale transcriptional activity in chromosomes 21 and 22. *Science* 296:916–919.
22. Rinn JL, et al. (2003) The transcriptional activity of human chromosome 22. *Genes Dev* 17:529–540.
23. Guttman M, Rinn JL (2012) Modular regulatory principles of large non-coding RNAs. *Nature* 482:339–346.
24. Rinn JL, Chang HY (2012) Genome regulation by long noncoding RNAs. *Annu Rev Biochem* 81:145–166.
25. Hu G, et al. (2013) Expression and regulation of intergenic long noncoding RNAs during T cell development and differentiation. *Nat Immunol* 14:1190–1198.
26. Necsulea A, et al. (2014) The evolution of lncRNA repertoires and expression patterns in tetrapods. *Nature* 505:635–640.
27. Engreitz JM, et al. (2013) The Xist lncRNA exploits three-dimensional genome architecture to spread across the X chromosome. *Science* 341:1237973.
28. Rinn JL, et al. (2007) Functional demarcation of active and silent chromatin domains in human HOX loci by noncoding RNAs. *Cell* 129:1311–1323.
29. Wang KC, Chang HY (2011) Molecular mechanisms of long noncoding RNAs. *Mol Cell* 43:904–914.
30. Bonasio R, Shiekhattar R (2014) Regulation of transcription by long noncoding RNAs. *Annu Rev Genet* 48:433–455.
31. Poliseno L, et al. (2010) A coding-independent function of gene and pseudogene mRNAs regulates tumour biology. *Nature* 465:1033–1038.
32. Satpathy AT, Chang HY (2015) Long noncoding RNA in hematopoiesis and immunity. *Immunity* 42:792–804.
33. Hu W, Yuan B, Flygare J, Lodish HF (2011) Long noncoding RNA-mediated anti-apoptotic activity in murine erythroid terminal differentiation. *Genes Dev* 25: 2573–2578.
34. Kotzin JJ, et al. (2016) The long non-coding RNA Morrbid regulates Bim and short-lived myeloid cell lifespan. *Nature* 537:239–243.
35. Gomez JA, et al. (2013) The NeST long ncRNA controls microbial susceptibility and epigenetic activation of the interferon-γ locus. *Cell* 152:743–754.
36. Huang W, et al. (2015) DDX5 and its associated lncRNA Rmrp modulate TH17 cell effector functions. *Nature* 528:517–522.
37. Atianand MK, et al. (2016) A long noncoding RNA lincRNA-EPS acts as a transcriptional brake to restrain inflammation. *Cell* 165:1672–1685.
38. Castellanos-Rubio A, et al. (2016) A long noncoding RNA associated with susceptibility to celiac disease. *Science* 352:91–95.
39. Heng TS, Painter MW; Immunological Genome Project Consortium (2008) The Immunological Genome Project: Networks of gene expression in immune cells. *Nat Immunol* 9:1091–1094.
40. Lattin JE, et al. (2008) Expression analysis of G protein-coupled receptors in mouse macrophages. *Immunome Res* 4:5.
41. Feng Y, et al. (2015) A mechanism for expansion of regulatory T-cell repertoire and its role in self-tolerance. *Nature* 528:132–136.
42. Wakamatsu E, Mathis D, Benoist C (2013) Convergent and divergent effects of costimulatory molecules in conventional and regulatory $CD4^+$ T cells. *Proc Natl Acad Sci USA* 110:1023–1028.
43. D'Alise AM, Ergun A, Hill JA, Mathis D, Benoist C (2011) A cluster of coregulated genes determines TGF-beta-induced regulatory T-cell (Treg) dysfunction in NOD mice. *Proc Natl Acad Sci USA* 108:8737–8742.
44. Sefik E, et al. (2015) Individual intestinal symbionts induce a distinct population of $ROR\gamma^+$ regulatory T cells. *Science* 349:993–997.
45. Kuczma M, et al. (2009) Foxp3-deficient regulatory T cells do not revert into conventional effector $CD4^+$ T cells but constitute a unique cell subset. *J Immunol* 183: 3731–3741.
46. Morikawa H, et al.; FANTOM Consortium (2014) Differential roles of epigenetic changes and Foxp3 expression in regulatory T cell-specific transcriptional regulation. *Proc Natl Acad Sci USA* 111:5289–5294.
47. Lin MF, Jungreis I, Kellis M (2011) PhyloCSF: A comparative genomics method to distinguish protein coding and non-coding regions. *Bioinformatics* 27:i275–i282.
48. Bonnal RJ, et al. (2015) De novo transcriptome profiling of highly purified human lymphocytes primary cells. *Sci Data* 2:150051.
49. Yang H, et al. (2013) One-step generation of mice carrying reporter and conditional alleles by CRISPR/Cas-mediated genome engineering. *Cell* 154:1370–1379.
50. Arvey A, et al. (2015) Genetic and epigenetic variation in the lineage specification of regulatory T cells. *eLife* 4:e07571.
51. Komatsu N, et al. (2009) Heterogeneity of natural $Foxp3^+$ T cells: A committed regulatory T-cell lineage and an uncommitted minor population retaining plasticity. *Proc Natl Acad Sci USA* 106:1903–1908.
52. Zorn E, et al. (2006) IL-2 regulates FOXP3 expression in human $CD4^+CD25^+$ regulatory T cells through a STAT-dependent mechanism and induces the expansion of these cells in vivo. *Blood* 108:1571–1579.
53. Schmidl C, et al.; FANTOM Consortium (2014) The enhancer and promoter landscape of human regulatory and conventional T-cell subpopulations. *Blood* 123:e68–e78.
54. Samstein RM, et al. (2012) Foxp3 exploits a pre-existent enhancer landscape for regulatory T cell lineage specification. *Cell* 151:153–166.
55. Sleutels F, Zwart R, Barlow DP (2002) The non-coding Air RNA is required for silencing autosomal imprinted genes. *Nature* 415:810–813.
56. Feuerer M, Shen Y, Littman DR, Benoist C, Mathis D (2009) How punctual ablation of regulatory T cells unleashes an autoimmune lesion within the pancreatic islets. *Immunity* 31:654–664.
57. Polansky JK, et al. (2008) DNA methylation controls Foxp3 gene expression. *Eur J Immunol* 38:1654–1663.
58. Buenrostro JD, Giresi PG, Zaba LC, Chang HY, Greenleaf WJ (2013) Transposition of native chromatin for fast and sensitive epigenomic profiling of open chromatin, DNA-binding proteins and nucleosome position. *Nat Methods* 10:1213–1218.
59. Tang Q, et al. (2008) Central role of defective interleukin-2 production in the triggering of islet autoimmune destruction. *Immunity* 28:687–697.
60. Carpenter S, et al. (2013) A long noncoding RNA mediates both activation and repression of immune response genes. *Science* 341:789–792.
61. Vignali DA, Collison LW, Workman CJ (2008) How regulatory T cells work. *Nat Rev Immunol* 8:523–532.
62. Liston A, et al. (2008) Differentiation of regulatory $Foxp3^+$ T cells in the thymic cortex. *Proc Natl Acad Sci USA* 105:11903–11908.
63. Bettelli E, et al. (2006) Reciprocal developmental pathways for the generation of pathogenic effector TH17 and regulatory T cells. *Nature* 441:235–238.
64. Ritchie ME, et al. (2015) limma powers differential expression analyses for RNA-sequencing and microarray studies. *Nucleic Acids Res* 43:e47.
65. Heinz S, et al. (2010) Simple combinations of lineage-determining transcription factors prime cis-regulatory elements required for macrophage and B cell identities. *Mol Cell* 38:576–589.
66. Ross-Innes CS, et al. (2012) Differential oestrogen receptor binding is associated with clinical outcome in breast cancer. *Nature* 481:389–393.
67. Krueger F, Andrews SR (2011) Bismark: A flexible aligner and methylation caller for Bisulfite-Seq applications. *Bioinformatics* 27:1571–1572.
68. Hebestreit K, Dugas M, Klein HU (2013) Detection of significantly differentially methylated regions in targeted bisulfite sequencing data. *Bioinformatics* 29: 1647–1653.
69. Siepel A, et al. (2005) Evolutionarily conserved elements in vertebrate, insect, worm, and yeast genomes. *Genome Res* 15:1034–1050.
70. Darce J, et al. (2012) An N-terminal mutation of the Foxp3 transcription factor alleviates arthritis but exacerbates diabetes. *Immunity* 36:731–741.
71. Hashimshony T, Wagner F, Sher N, Yanai I (2012) CEL-Seq: Single-cell RNA-Seq by multiplexed linear amplification. *Cell Reports* 2:666–673.
72. Meredith M, Zemmour D, Mathis D, Benoist C (2015) Aire controls gene expression in the thymic epithelium with ordered stochasticity. *Nat Immunol* 16:942–949.
73. Kim D, et al. (2013) TopHat2: Accurate alignment of transcriptomes in the presence of insertions, deletions and gene fusions. *Genome Biol* 14:R36.
74. Anders S, Pyl PT, Huber W (2015) HTSeq—a Python framework to work with high-throughput sequencing data. *Bioinformatics* 31:166–169.
75. Cong L, et al. (2013) Multiplex genome engineering using CRISPR/Cas systems. *Science* 339:819–823.
76. Martin M (2011) Cutadapt removes adapter sequences from high-throughput sequencing reads. *EMBnet J* 17:10–12.
77. Langmead B, Salzberg SL (2012) Fast gapped-read alignment with Bowtie 2. *Nat Methods* 9:357–359.

Supporting Information

Zemmour et al. 10.1073/pnas.1700946114

SI Materials and Methods

Mice. C57BL/6J mice were obtained from The Jackson Laboratory. NOD/Lt/DOI and Foxp3-DTR-GFP/N (56), Foxp3-Ires-Thy1.1/B6 (62), and Foxp3-IRES-GFP/B6 (63) mice were maintained in our colony. Foxp3-DTR-GFP/N mice carry a BAC transgene encompassing 150 kb downstream and 70 kb upstream of the *Foxp3* TSS. DTR-eGFP with a stop codon was inserted between the first and second codons of Foxp3. All experimentation was performed following animal protocol guidelines of Harvard Medical School (reviewed and approved HMS IACUC protocols 02954).

Flow Cytometry. Single-cell suspensions from lymphoid organs were generated by physical dissociation through a 40-μm cell strainer (Falcon). Red blood cells were lysed with ACK lysing buffer (Lonza) for 2 min on ice. For pancreas-infiltrating cells, mice were perfused before harvest via injection of ∼10 mL of PBS into the heart. Careful inspection ensured removal of visible lymph nodes. The pancreas was minced in small pieces in 500 μL of digestion buffer [DMEM-2% FBS + collagenase IV 1 mg/mL (Gibco; 17104–019) and DNase1 10 U/mL (Sigma-Aldrich; DN25)] and digested in 25 mL of digestion buffer at 37 °C for 20 min at 500 × *g*. After filtering through a 10-μm cell strainer (Falcon), cold medium (DMEM-2% FBS) was added, and then cells were pelleted by centrifugation at 500 × *g* for 15 min. ACK lysis (500 μL) was performed for 1 min on ice, followed by filtration through a 50-μm cell strainer, washing for 5 min at 500 × *g*, and resuspension in 200 μL of PBS (DMEM-2% FBS). Cells were stained on ice for 5–10 min in the dark in FACS buffer (DMEM without phenol red-2% FBS) with antibodies against CD4 (GK1.5; BioLegend), CD25 (PC61; BioLegend), TCRβ and (H57-597; BioLegend). Foxp3 staining was performed in accordance with the manufacturer's protocol with an anti-Foxp3 mAb (FJK-16S; eBiosciences). Permeabilization and staining were done at room temperature for 30 min.

Antibody staining was performed for 20 min at 4 °C in PBS with the following antibodies (1/200 dilution unless noted otherwise): CD45 (PB, clone 30-F11; BioLegend), TCRβ (PE-Cy7, clone H57-597; BioLegend), CD25 (FITC, clone PC61; eBioSciences), CD4 (V500, clone RM4.5; BD Biosciences), CD8 (PE, clone 53–6.7; BioLegend), and LiveDead Fixable Near IR (1/1000; Life Technologies). After permeabilization/fixation for 2 h on ice, Foxp3 staining (APC, clone FJK-16S; eBiosciences) was performed for 30 min at room temperature in the dark in accordance with the manufacturer's instructions.

Data were recorded on an LSRII flow cytometer (BD Biosciences) and analyzed using FlowJo version 9.3.2. Foxp3 MFI was calculated using a FlowJo internal function. The percentage of Foxp3-low cells was calculated as the proportion of cells with 50% Foxp3 expression compared with the average normalized to CD25 expression, as shown in the gates.

Mapping of Mouse *Flicr* Transcripts. We performed 5′ RACE using the SMARTer RACE cDNA Amplification Kit, and Sanger-sequenced the product. The 5′ extremities were also confirmed with FANTOM CAGE data (46). The 3′ termini were mapped by 3′ RACE and 3′ end RNA-Seq. Exploratory PCR was performed using primers spanning the 4930524L23Rik locus (Fig. S2). Isoforms were cloned with primers designed based on the extremities found. PhyloCSF (47) was used to predict low peptide coding potential for all *Flicr* and *FLICR* transcripts.

Mapping of 5′ and 3′ termini by RACE. To prepare Treg RNA, we sorted 2–3 × 10^5 $CD4^+$ $TCR\beta^+$ $Thy1.1^+$ Tregs from Foxp3-Ires-Thy1.1/B6 mice on a FACSAria II cell sorter (BD Biosciences) into 500 μL of TRIzol LS. RNA was extracted using the Direct-zol RNA MiniPrep Kit (Zymo Research).

We performed 5′ and 3′ RACE using the SMARTer RACE cDNA Amplification Kit (Clontech). cDNA was synthesized as described in the kit using 5′ and 3′ RACE CDS primers and SMARTer IIA oligo for template switching for 5′ RACE. cDNA ends were then amplified by nested touchdown PCR. The first PCR used Universal Primer A mixed with TD_R1 = TGGCAGCTGCGTGTCCTCGATTTGGC for the 5′ ends or TD_F1 = TGCAAAGAGGTGGTGGTGGCCATGCAG for the 3′ ends: 5 cycles of 94 °C for 30 s and 72 °C for 4 min → 5 cycles of 94 °C for 30 s, 70 °C for 30 s, and 72 °C for 4 min → 25 cycles of 94 °C for 30 s, 68 °C for 30 s, and 72 °C for 4 min. The second nested PCR used Nested Universal Primer A and TD_R2 = CTGCATGGCCACCACCACCTCTTTGCA for the 5′ ends or TD_F2 = TGGTTACAGGGAGCCGGTCTGTGCCA for the 3′ ends; 5 cycles of 94 °C for 30 s and 72 °C for 4 min → 5 cycles of 94 °C for 30 s, 70 °C for 30 s, and 72 °C for 4 min → 25 cycles of 94 °C for 30 s, 68 °C for 30 s, and 72 °C for 4 min. Fragments were purified after agarose gel electrophoresis with the QiaQuick Gel Extraction Kit (Qiagen) and cloned in TOPO-TA pCR-2.1 (Invitrogen), and the inserts were sequenced.

Mapping of 3′ termini by RNA-Seq. Because it involves oligo-dT priming and sequencing of 3′ UTR tags, RNA-Seq performed as described by Hashimshony et al. (71) yielded additional information on the polyadenylation site of *Flicr* transcripts. RNA-Seq was performed as detailed elsewhere (72). In brief, first-strand cDNA synthesis was performed using a barcoded oligonucleotide primer, which included an oligodT sequence, a sample barcode, and a T7 promoter for later amplification. Second-strand cDNA synthesis was performed using the NEBNext mRNA Second-Strand Synthesis Module (New England BioLabs). After Agencourt AMPure XP bead size selection and purification, in vitro transcription was performed overnight with the MEGAshortscript T7 Transcription Kit (Ambion). The amplified RNA was fragmented using the NEBNext Magnesium RNA Fragmentation Module (New England BioLabs), purified with AMPure beads, and treated with phosphatase and T4 polynucleotide kinase before ligation with an Illumina 3′ adapter. Ligated RNA was then reverse-transcribed. P5 and P7 Illumina sequences were added by PCR. Libraries were size-selected and sequenced on an Illumina HiSeq 2500 system.

Reads were filtered for quality using the FASTX toolkit, version 0.0.13 (fastq_quality_filter -v -Q 33 -q 20 -p 80). Mapping to the mm10 reference genome and transcriptome was performed using Tophat2 (73), conserving the strand information (tophat -p 2 -library-type fr-firststrand -read-mismatches 5 -read-gap-length 5 -readedit-dist 5 -no-coverage-search -segment-length 15 –transcriptome-index).

TruSeq RNA sequencing. Here 10^5 $CD4^+TCR\beta^+GFP^+$ Tregs and GFP^- Tconvs from 6-wk-old Foxp3-IRES-GFP/B6 mice were double-sorted in biological duplicates on a BD FACSAria II into 500 μL of TRIzol LS. RNA was extracted as follows. RNA was separated by adding 100 μL of chloroform, mixing and spinning at 12,000 × *g* for 15 min at 4 °C. The aqueous phase containing the RNA was harvested, and 1 μL of Glycoblue (Ambion) was added. RNA was then precipitated by adding 1 volume of isopropanol, followed by incubation for 1 h at −80 °C. It was then washed with 70% ethanol and resuspended in nuclease-free water.

Illumina libraries were constructed with the TruSeq RNA Sample Preparation V2 LS Kit, in accordance with the manufacturer's instructions, with two modifications. After ligation, DNA fragments were size-selected by gel electrophoresis (150–

300 bp), and 17 cycles of PCR were performed using Phusion High-Fidelity PCR Master Mix with HF Buffer (Thermo Fisher Scientific). Libraries were sequenced on an Illumina HiSeq 2000 instrument. Reads were filtered for quality using the FASTX toolkit, version 0.0.13 (fastq_quality_filter -v -Q 33 -q 20 -p 80). Mapping was performed using Tophat2 (73) on the mm9 transcriptome and genome using default parameters.

Exploratory PCR. RNA from 5×10^4 $CD4^+TCR\beta^+GFP^+$ Tregs from Foxp3-IRES-GFP/B6 sorted and prepared as above was used for cDNA synthesis with SuperScript II enzyme (Invitrogen) and oligodT following the manufacturer's instructions. PCR analyses were performed using primer pairs spanning the 4930524L23Rik locus, as shown in Fig. S2*A*. The primers were designed to encompass regions identified by RACE and RNA-Seq, as well as putative regions suggested by the ESTs or probing introns between *Ppp1r3f* and *Foxp3*.

Synthesis by PCR. Primers were designed following the extremities of 3′ and 5′ ends identified by RACE and 3′ RNA-Seq, as diagramed in Fig. S2*A*. All primer combinations were used, and fragments resulting from successful amplification were cloned into the TOPO-TA pCR-2.1 vector (Invitrogen) and sequenced. Four isoforms of *Flicr* were identified in this manner (Fig. 2*A* and Fig. S2*A*).

Mapping of Human *Flicr* Transcripts. Essentially similar techniques were used to map the human *FLICR* transcripts, using RNA prepared from the $FOXP3^+$ C5/MJ HTLV1-transformed cell line (ATCC CRL-8293), cultured in Iscove's modified Dulbecco's medium supplemented with 20% FBS and penicillin-streptomycin.

RACE. We performed 5′ and 3′ RACE using the same protocol as described above. Nested touchdown PCR was performed with the following primers designed in the conserved DNA region between mouse and human:

5′ reaction 1: h_F2 = CACAGAGCTGGCGAGTGTGGGTCCC for PCR1, then h_F5 = TGACCTCAGCAGGCACTCTA for PCR2

5′ reaction 2: h_F5 = TGACCTCAGCAGGCACTCTA for PCR1, then h_F3 = GGATGAGCCAATGCCGAGG for PCR2

3′ reaction: h_R5 = TCTCAGTAGCTGATGTTTATCTTGAATT for PCR1, then h_R4 = GGTGAAGGGGTGGATCTTGG for PCR2.

RNA-Seq. We reanalyzed the human RNA-Seq data published by Bonnal et al. (48), using tophat2 to map the data to a custom-made transcriptome reference derived from Hg19 and supplemented with *FLICR*. After removing PCR duplicates using the Picard tool MarkDuplicates (picard.sourceforge.net), we obtained gene counts using htseq-count (htseq-count -f bam -r pos -s no -t exon -i gene_id -m union) (74) and a custom GTF file supplemented with *FLICR* annotation. Data were normalized to the length of the genes and the library size in fragments per kb per million reads using a custom R script.

Synthesis by PCR. Primers were designed following the extremities of 3′ and 5′ ends identified by RACE. All primer combinations were performed by PCR and fragments were cloned in TOPO-TA pCR-2.1 (Invitrogen) and sequenced. Three isoforms of *FLICR* were identified with h_F2 and h_R5.

Construction of a *Flicr* KO Mouse. We closely followed the methods described by Yang et al. (49) to generate *Flicr*-deficient mice using the CRISPR/Cas9 system, with a few modifications. Because the active region of *Flicr* is unknown, we chose to introduce a point mutation at the shared splice donor site (*Flicr* mutant 1) or to delete a whole exon (exon 2) encompassing the region of highest homology between mouse and human transcripts, but keeping the mutation as small as possible to avoid interfering with *Foxp3* enhancer elements (*Flicr* mutant 2).

For gRNA selection, we followed the protocol published by Cong et al (75) for the design and cloning of gRNAs (www.genome-engineering.org/crispr/wp-content/uploads/2014/05/CRISPR-Reagent-Description-Rev20140509.pdf), with the following criteria: (*i*) 20–21 bp complementary to the target region on the sense or antisense strand; (*ii*) flanked in 3′ with a PAM sequence (NGG); (*iii*) no/few off-targets predicted by alignment with bowtie (bowtie -a–best -v 0 -c mm9 gRNA with all four possible PAM sequences). For *Flicr* mutant 1, we used GCAAGACTGGCTTCAGGCCTG (gRNA_1) targeting the acceptor spliced site on exon 3. For *Flicr* mutant 2, we used GCCTGTGTGGTGCCTGGAAGC (gRNA_2a) and CAAAAAGGTGAGTTAAGATG (gRNA_2b) flanking *Flicr* exon 2. We cloned the gRNAs in the pX330 vector following the protocol (75). In brief, gRNA oligos were synthesized with BbsI overhangs caccGCAAGACTGGCTTCAGGCCTG+aaacCAGGCCTGAAGCCAGTCTTGC for gRNA_1, caccGCCTGTGTGGTGCCTGGAAGC+aaacGCTTCCAGGCACCACACAGGC for gRNA_2a, and caccGCAAAAAGGTGAGTTAAGATG+aaacCATCTTAACTCACCTTTTTGC for gRNA_2b; annealed; phosphorylated; ligated to the pX330 vector (75) previously digested with BbsI; and gel-purified using the QiaQuick Gel Extraction Kit (Qiagen). DH5alpha bacteria were transformed with the ligation product (30 min on ice, 42 °C for 30 s, 30 s on ice) and spread on ampicillin LB agar plates. Clones were hand-picked and sequenced after MiniPrep (Invitrogen).

gRNA was prepared following Yang et al. (49). T7 promoter was added to the gRNAs by PCR using forward primers TAATACGACTCACTATAGGCAAGACTGGCTTCAGGCCTG (gRNA_1), TAATACGACTCACTATAGGCCTGTGTGGTGCCTGGAAGC (gRNA_2a), and TAATACGACTCACTATAGGCAAAAAGGTGAGTTAAGATG (gRNA_2b) and reverse primer AAAAGCACCGACTCGGTGCC (tracr_R). The gRNAs were then transcribed in vitro from the PCR amplicons (150 nM final) using the MEGAshortscript T7 Kit (Life Technologies), and the RNA was purified using the MEGAclear Kit (Life Technologies).

For *Flicr* mutant 1, the ssDNA oligonucleotide AGGCTTCCAGCCTTTGGTGCCCTGGCATCCTGCAGAGAGCTAAGAGTTCCAGGTATCCAGGATCCGAGGAAGAGAAAGTAGAAATACGTTTTTATTCACATGATGCTAACCTAGTAAACAATTCC was designed to delete 45 bp and introduce a novel BamHI site.

For *Flicr* mutant 2, through several rounds of PCR, we constructed and cloned into the TOPO-TA pCR-2.1 vector (Invitrogen) a recombinant dsDNA substrate for homologous recombination, designed to delete 245 bp and introduce an artificial EcoRI site (GAATTC): CCCATTACCTGTTAGGTATGCTCTTCACCCCTCCCCTATTCCCTCCCACACACAACCACAACTGTTAAGCTCCTAAGATCCATGCAGACCTCCAAAGTAAGAGGACCTCATCCCACCTCTGCCCCTCCCTCCCTCTCAACTCAGGACCTCCCCCGGCT**GAATTC**ATGAGGAAAGTCAGTCTCTTTTTTGTTGTTGTTGTTGGGGCGGGGGGAGGTGCTCAGAAGATAGCCGAAAGGGACAAAAAGTGCAAATGAGGGAAAGAGCAAAGGAGTGTGGGAATTGTTTACTAGGTTAGCATCATGTGAATAAAAACGTATTTCTACTTTCTCTTCCTCAGGCCTGAA. dsDNA substrate was amplified by PCR from this plasmid, gel-purified, and resuspended in microinjection buffer.

Cas9 protein was purchased from TriLink Biotechnologies (L-6325).

Zygote microinjection. Here 8- to 10-wk-old NOD females were used as donors of fertilized zygotes. Superovulation was induced by two injections of 2.5 IU of pregnant mare serum gonadotropin/human chorionic gonadotropin given 47.5 h apart. gRNA, Cas9 mRNA, and HR substrate were suspended just before injection in a microinjection buffer (10 mM Tris/0.1 mM EDTA, pH 7.4) at a concentration of 5, 2.5, and 5 ng/μL, respectively. Microinjection was performed into the male pronucleus, and surviving embryos were implanted directly in pseudopregnant NOD females.

The founder female for *Flicr* mutant 1 had a 12-bp deletion with a 17bp insertion containing the BamH1 site:

CTACTTTCTCTTCCTC**GGATCCTGGATCGAAGC**CAGTC-TTGCAAAGAGG.

This founder gave rise to one mutant male, but no further progeny could be obtained.

The founder male for *Flicr* mutant 2 had a 263-bp deletion including exon 2 (mm9 chrX:7154602–7154865): CCTCCCTCTCAACTC-AG-**263-bp DELETION-**GAAAGTCAGTCTCTTT. This founder gave rise to multiple progeny in the expected ratio from Mendelian segregation of the ChrX. Progeny were genotyped by PCR with the following primer combinations: WT PCR using F, AGT-GAAAGTTTTGCTTTGAACTAATGAT and R, TACAGA-CGAGCCTCCACAGA; KO PCR using F, AACTGTCTCAGA-GACATAGAAGATACAG and R, AGAGACTGACTTTCCT-GAGTTGAGA.

Bone Marrow Chimera Experiments. *Rag*-KO NOD mice were irradiated with 5 Gy and reconstituted with equal proportions of congenically labeled T cell-depleted bone marrow cells from WT (CD45.2) and KO (CD45.1) mice. Bone marrow cells were harvested from both femurs and tibias of NOD CD45.1 (*Flicr* KO) and CD45.2 (WT) mice. After red blood cell lysis with ACK, T cells were depleted as follows. Bone marrow single-cell suspensions were incubated with biotinylated anti-CD3e antibodies for 5 min in MACS buffer, washed, and then incubated with 100 μL of streptavidin beads (Dynabeads Biotin Binder, 11047; Thermo Fisher Scientific) for 20 min. Isolation of the $CD3^-$ population was performed after three magnet incubations for 2 min. A total of 4 million cells (2 million CD45.1 and 2 million CD45.2) were injected i.v. in each mouse. Mice were treated for 2 wk with trimethoprim-sulfamethoxazol and analyzed 10 wk later.

In Vitro FoxP3 Stability. Tregs from spleen and subcutaneous lymph nodes were prepared by magnetic negative selection (using PE-conjugated antibodies against CD8a, CD11b, CD11c, CD19, NK1.1, and Ter119 anti-PE MACS microbeads; Miltenyi Biotec); stained with mAbs against CD4, TCRβ, and CD25, with DAPI (1 μg/mL) as a viability dye; and then sorted by flow cytometry on a FACSAria II cell sorter into 500 μL of complete medium. Cells were then cultured at 37 °C and 5% CO_2 in 200 μL of complete RPMI medium with anti-CD3/CD28 beads (1:1 bead:cell ratio; Dynabeads Mouse T-Activator CD3/CD28; Gibco) and various concentrations of IL-2 (recombinant human IL-2, 212–12; Peprotech).

RT-qPCR. RNA was extracted using TRIzol LS and the Direct-zol RNA MiniPrep Kit (Zymo Research) and eluted in 25 μL of RNase-free water. Then 10 μL of RNA was used for reverse transcription with SuperScript III (Invitrogen) using oligo-dT primers. cDNA (4 μL) was used for qPCR in a 20-μL reaction with SYBR Green PCR Master Mix on the StepOnePlus Real-Time PCR System (Applied Biosystems) using the following primers: Acting1_F, TTGCCTTGAGTTGGGAACGT, Acting1_R, CAC-AATGACGTGTTGCTGGG; Foxp3_F, GTGCACGTACAC-ACATGCAG, Foxp3_R, TAGGCATGGATTGGGGCTTG; Flicr_F, CAAGCCATCAGTTCCAGTCTT, Flicr_R, CTGA-CAAGGCACGGCTAAG. Gene expression is represented as $2^{-\Delta Ct}$ (ΔCt = Ct_target − Ct_Actg1).

RNAi Using LNA GapmeRs. Total CD4 T cells from spleen and subcutaneous lymph nodes were isolated by magnetic negative selection (Dynabeads Untouched Mouse CD4 T-Cell Kit, 11415D; Thermo Fisher Scientific) and activated in vitro in 200 μL of cRMPI for 72 h with anti-CD3/CD28 beads in a 96-well plate (0.1 M cell/well, 1:1 bead:cell ratio; Dynabeads Mouse T-Activator CD3/CD28; Thermo Fisher Scientific) and 50 U/mL IL-2 (recombinant human IL-2, 212–12; Peprotech).

After 72 h, cells were transfected with five different types of LNA targeting the common region of *Flicr* (exons 2 and 3) and a negative control LNA and GFP plasmid using the Lonza 4D-Nucleofector System and the protocol for mouse T cells (Amaxa 4D Nucleofector Protocol and Kit, V4XP-3024; Lonza). Activation beads were removed using a magnet, and activated cells were pelleted and resuspended in 100 μL of supplemented nucleofector solution. A total of 1 million cells per condition were used. After 500 pmol of LNA was added to the cells, the cells were transfected using the DN-100 program, followed by the immediate addition of 500 μL of prewarmed complete RPMI.

After 24 h of incubation in complete RPMI supplemented with 100 U/L IL-2, FoxP3 expression was assessed by flow cytometry as described above.

LNA sequences (standard desalted, phosphorothioate backbone) (Exiqon): G*C*T*T*A*A*G*A*T*C*A*C*A*A*T*T
T*A*A*C*A*A*G*A*C*T*G*G*A*A*C
G*G*A*A*C*T*G*A*T*G*G*C*T*T*G*G
C*T*C*A*T*C*T*T*A*A*C*T*C*A*C
T*T*T*A*G*A*C*C*G*A*T*G*G*G*C*A
Antisense LNA GapmeR negative control A (300610; Exiqon).

ATAC-seq. ATAC-seq was performed in biological duplicates following the protocol described by Buenrostro et al. (58). In brief, 50,000 $CD4^+TCR\beta^+CD25^{hi}$ (top 50%) Tregs were sorted and lysed. After transposition and PCR, a final bead purification and selection (100–600 bp) was performed twice using 0.6× and 1.6× SPRI beads. Libraries were paired-end sequenced (40, 50) using a 75-bp kit on an Illumina NextSeq high-throughput sequencing system.

Fastq reads were first filtered on quality using sickle 1.2 (sickle pe -f R1.fastq -r R2.fastq -o filtered_R1.fastq -p filtered_R2.fastq -t sanger -s filtered_singles.fastq). Then adapters were trimmed using cutadapt 1.8.1 (76) (cutadapt -a AGATGTGTATAAGA-GACAG -A CTGTCTCTTATACACATCT -o clean_R1.fastq -p clean_R2.fastq filtered_R1.fastq filtered_R2.fastq), and reads were mapped against mm9 mouse genome using bowtie2 (77) (bowtie2 -p 2 -x mm9 -X 1000–fr -1 clean_R1.fastq -2 clean_R2.fastq -S btout2.sam). Reads mapping to more than one location were discarded using the XS field (sed '/XS:/d' mapped.sam > mapped_1alignmentonly.sam). PCR duplicates were removed using Picard tools 1.130 (java -Xms1024m -jar /opt/picard-1.130/picard.jar MarkDuplicatesWithMateCigar INPUT = mapped_1align.sorted.bam OUTPUT=$prefix.sorted.uniq.bam METRICS_FILE = metrics.txt REMOVE_DUPLICATES = true ASSUME_SORTED = true SKIP_PAIRS_WITH_NO_MATE_CIGAR = true). Nucleosome-free fragments (<120 bp) were isolated (samtools view -h $prefix.sorted.uniq.bam | awk ' /^@/ { print $0 >> "nuc120.sam" ; next } { if ($9 <120 && $9 > -120) {print $0 >> "nuc120.sam"} }'). Finally, peaks were called using Homer 4.6 (findPeaks homer_tagdir_nuc120/ -o $prefix.nuc120.peaks_size250mindist500.txt -region -size 250 -minDist 500) (65). Data were imported in R, and differential peak analysis was performed using DiffBind (i.e., differential peak analysis based on negative binomial distributions) (66). DiffBind calculates *P* value for each peak based on the genome wide distribution of differences (following a negative binomial distributions).

Methylation Analysis of the Foxp3 Locus by Bisulfite Treatment and Illumina Sequencing. The protocol was adapted from Feng et al. (18) for Illumina sequencing. A total of 80,000 $CD25^{hi}$ Tregs were sorted as above, DNA was purified, and bisulfate-converted using the EZ DNA Methylation Direct Kit (Zymo Research). Bisulfate-converted regions were then amplified by PCR. Illumina adapters were ligated and libraries amplified by a final PCR before sequencing on an Illumina MiSeq system.

Adapters. PE_adapter_top: ACACTCTTTCCCTACACGACGCTCTTCCGATC*T (*phosphorothiate linkage). PE_adapter_bottom: pGATCGGAAGAGCACACGTCT (p, 5′ phosphate). Oligos were dissolved in low-TE buffer to generate 100 μM stock for each oligo. To generate 200 μL of 15 μM adapters, we added 30 μL of the top and bottom oligos to a 1.5-mL Eppendorf tube with 2 μL of 5 M NaCl and 138 μL of low-TE buffer. The reaction incubated in a 98 °C water bath for 5 min, after which the water bath was turned off and the solution was slowly brought to room temperature. Annealed adapters were stored at −80 °C for 2 y.

Bisulfate conversion was done following the instructions in the EZ DNA Methylation Direct Kit (Zymo Research) and eluted in 22 μL.

Primers: meth_−1.5 kb_F, TGTTAGGGTATTAAAGGTTGGAAGTT; meth_−1.5 kb_R, CCAATTTTCCTAAAACCAACAATAT; meth_promA_F, AAAAATTTAAAATTTTAAAATTTT; meth_promA_R, AAAAAACTACCACATTATCAAAAACAACT; meth_promB_F, TATATTTTTAGATGATTTGTAAAGGGTAAA; meth_promB_R, ATCAACCTAACTTATAAAAAACTACCACAT; meth_CNS2A_F, TTTTGGGTTTTTTTGGTATTTAAGA; meth_CNS2A_R, ACAAATAATCTACCCCACAAATTTC; meth_CNS2B_F, TGGGTTTTTTTGGTATTTAAGAAAG; meth_CNS2B_R, AAAAAACAAATAATCTACCCCACAA; meth_CNS2C_F, TTTGGGTTTTGTATGGTAGTTAGATG; meth_CNS2C_R, CACAACCTAAACTTAACCAAATTTTTC; meth_CNS2D_F, GTGGGGTAGATTATTTGTTTTTTTT; meth_CNS2D_R, AACCAACCAACTTCCTACACTATCTAT; meth_CNS2flank_F, ATGAAGTATTATAAATTGGGGGATTTATAT; meth_CNS2flank_R, AAAACTAAAACTAACTTCCTAAAACC; meth_exon4_F, TTTGTTGTAGTTGTTTTTGTTAAAAATTTA; meth_exon4_R, CCAATAACTTAAACATAACCTCACAAA; meth_exon11_F, TGAAAGGTTATAATGAAATGATAAGTTTAA; meth_exon11_R, ATTACCATAACTTCCCCAAAAATAC; meth_exon14_F, TTTGAGTTTGTATAAGTGTTTTTGTG; meth_exon14_R, CCCACCTTTTCTTAATTTTAAAATC.

PCR. Epitaq (Takara) was used for amplification of bisulfate-converted regions. For the −1.5 kb promoter B, CNS2a/b/c/d/flank, and exon 8, PCR reactions were as follows: Epitaq (5 U/μL), 0.25 μL; 10× buffer (Mg-free), 5 μL; $MgCl_2$ (25 mM), 5 μL; dNTPs (2.5 mM each), 6 μL; DNA, 1 μL; primer_F (10 μM), 2 μL; primer_R (10 μM), 2 μL; water, 28.75 μL. Forty cycles of 98 °C for 10 s, 55 °C for 30 s, and 72 °C for 30 s. For exons 4 and 14, PCR reactions were as follows: Epitaq (5 U/μL), 0.25 μL; 10× buffer (Mg-free), 5 μL; $MgCl_2$ (25 mM), 5.5 μL; dNTPs (2.5 mM each), 6 μL; DNA, 1 μL; primer_F (10 μM), 2 μL; primer_R (10 μM), 2 μL; water, 28.75 μL. Forty cycles of 98 °C for 10 s, 50 °C for 30 s, and 72 °C for 30 s. All PCR reactions from the same sample were then pooled, purified, and size-selected using 1.8× SPRI beads.

Ligation. Adapter ligation (DNA:adapter, 1:30) was performed for 15 min at 25 °C with the Quick Ligation Kit (New England BioLabs): Buffer 2× , 29 μL; DNA (1 μg = 6.5 pmol) adapter (100 μM), 2 μL (200 pmol); Quick T4 DNA Ligase, 5 μL; water, 18 μL.

PCR. DNA was purified with 1.8× SPRI beads and the last PCR adding Illumina P5–P7, and indexing was performed as follows: KAPA 2x mix, 25 μL; PE1.0, 1 μL; PE2.X indexed primer, 1 μL; DNA, 18 μL; water, 5 μL. 95 °C for 3 min, then five cycles of 98 °C for 20 s, 65 °C for 20 s, and 72 °C for 20 s, and then a final elongation step at 72 °C for 1 min. PE1.0: AATGATACGGCGACCACCGAGATCTACACTCTTTCCCTACACGACGCTCTTCCGATC*T; PE2.1: CAAGCAGAAGACGGCATACGAGATCGTGATGTGACTGGAGTTCAGACGTGTGCTCTTCCGATC*T; PE2.2: CAAGCAGAAGACGGCATACGAGATACATCGGTGACTGGAGTTCAGACGTGTGCTCTTCCGATC*T; PE2.3: CAAGCAGAAGACGGCATACGAGATGCCTAAGTGACTGGAGTTCAGACGTGTGCTCTTCCGATC*T; PE2.4: CAAGCAGAAGACGGCATACGAGATTGGTCAGTGACTGGAGTTCAGACGTGTGCTCTTCCGATC*T; PE2.5: CAAGCAGAAGACGGCATACGAGATCACTGTGTGACTGGAGTTCAGACGTGTGCTCTTCCGATC*T; PE2.6: CAAGCAGAAGACGGCATACGAGATATTGGCGTGACTGGAGTTCAGACGTGTGCTCTTCCGATC*T; PE2.7: CAAGCAGAAGACGGCATACGAGATGATCTGGTGACTGGAGTTCAGACGTGTGCTCTTCCGATC*T; PE2.8: CAAGCAGAAGACGGCATACGAGATTCAAGTGTGACTGGAGTTCAGACGTGTGCTCTTCCGATC*T.

Libraries were purified with 1.8× SPRI beads and paired-end sequenced by MiSeq (Nano Kit; 150–150).

Analysis. Reads were trimmed of the adapter using trim_galore–fastqc–paired–trim1–retain_unpaired–adapter AGATCGGAAGAGCACACGTCT–a2 AGATCGGAAGAGCACACGTCT *R1.fastq *R2.fastq. Then alignment to the mm9 genome was performed using Bismark (67) (bismark -p 2 -q–non_directional–bowtie2 mm9 -1 *R1_val_1.fq -2 *R2_val_2.fq). Data were analyzed and visualized using custom R scripts and the BiSeq library (68).

Autoimmune Diabetes. KO females and their heterozygous littermates were screened for diabetes by glucose urinalysis (Diastix strips) every week for 30 wk. Positive strip tests were confirmed by blood analysis, and animals with serum glucose >250 mg/dL on 2 consecutive days were considered diabetic. Diabetes incidence comparison was done using the Mantel–Cox log-rank test. For histological evaluation, pancreas tissues were fixed in formalin, embedded in paraffin, and stained with hematoxylin and eosin. Four-step sections separated by 100 μm were used to calculate the insulitis score for each islet (0, no infiltration; 1, peri-insulitis; 2, intraislet insulitis), and 100 independent islets were scored for each mouse.

Accession Data. ImmGen consortium (GSE15907 and GSE37448), GNF Mouse GeneAtlas V3 GSE10246 (40), GSE42276 (42), GSE57272 (19, 43), GSE68009 (44), GSE11775 (45), GSE71309 (41), Atlas of Human Lymphocytes E-MTAB-2319 (48), GSE43119 (53), Treg FANTOM CAGE data (46).

Statistics and Data Visualization. Statistical significance was assessed using all data and ANOVA to control for the confounding effect of the date of the experiments. The paired Student *t* test was used for the bone marrow chimera experiments. Diffbind was used for ATAC-seq. For correlations, Fisher *z*-transformation was applied. $P < 0.05$ was considered significant.

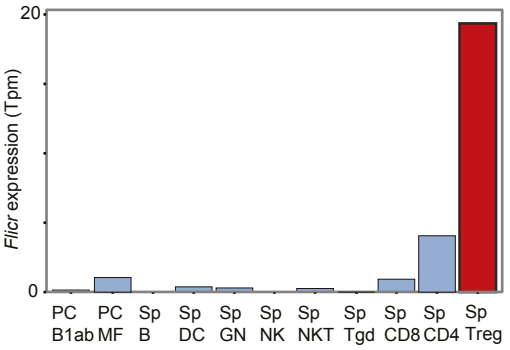
20
0
Filcr expression (Tpm)
PC B1ab
PC MF
Sp B
Sp DC
Sp GN
Sp NK
Sp NKT
Sp Tgd
Sp CD8
Sp CD4
Sp Treg

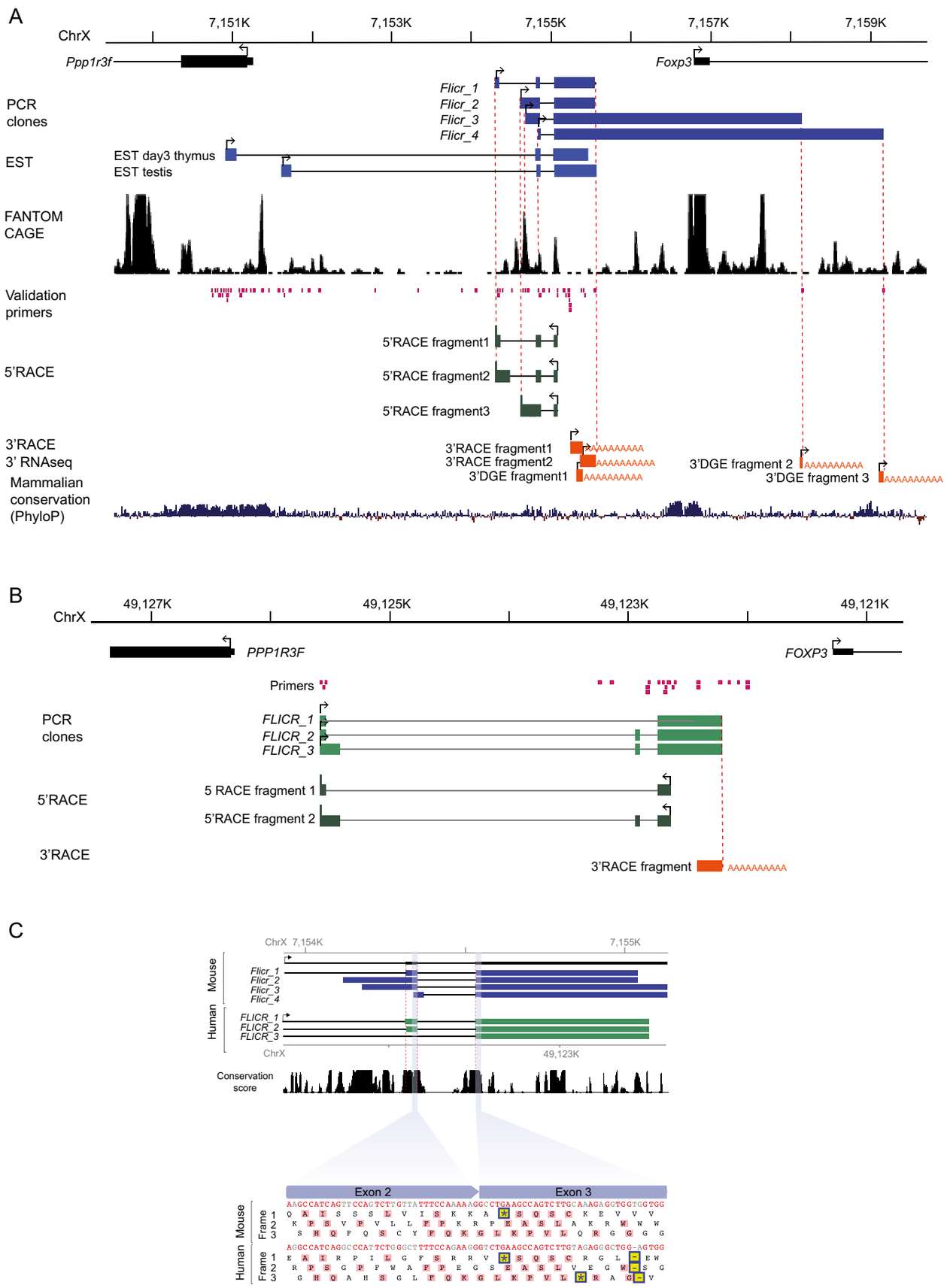

Fig. S2. *Flicr* expression and structure in mice and humans. (*A*) Map of *Flicr* in the mouse genome (mm9 coordinates). From top to bottom: Refseq annotation; PCR clones of *Flicr* isoforms; EST from the thymus and testis; FANTOM CAGE pile-up reads (46); primers used for exploratory PCRs designed to encompass regions identified by RACE and RNA-Seq but also putative regions suggested by the ESTs or probing introns between *Ppp1r3f* and *Foxp3*; 5′ RACE fragments; 3′ RACE fragments and 3′ RNA-Seq reads; mammalian conservation (PhyloP) (69). (*B*) Map of *Flicr* in the human genome (hg19 coordinates). From top to bottom: Refseq annotation; primers used in exploratory PCRs designed to encompass regions identified by RACE but also probing introns between *PPP1R3F* and *FOXP3*; PCR clones of *Flicr* isoforms; 5′ RACE fragments; 3′ RACE fragments. (*C*) Map of *Flicr* in the mouse (blue) and human (green) *FOXP3* loci (mm9 and hg19 coordinates), shown at three different levels of resolution, with PhastCons placental mammal sequence conservation score (69). At the bottom is the alignment of mouse and human transcripts in the conserved region of exons 2 and 3 and translation in the three frames. Although this region is conserved across placental mammals (red bases or amino acids), we did not find any conserved peptide sequences between human and mouse in any of the three frames, arguing against purified selection for a specific peptide sequence. PhyloCSF scores were accordingly low (47).

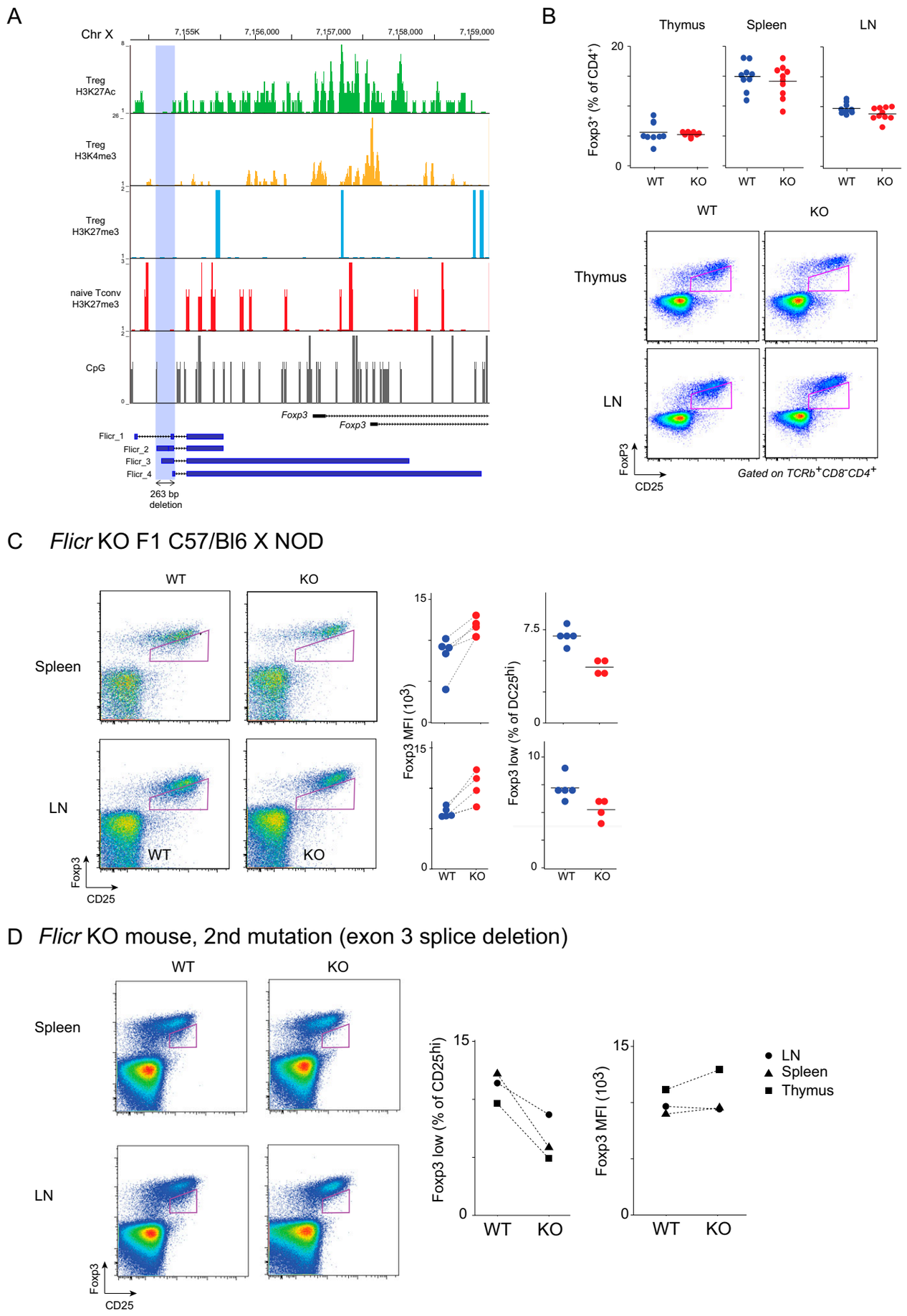

Fig. S3. Deletion of *Flicr* in the epigenome context of the *Foxp3* locus context and its effect in the autoimmune-resistant B6xNOD mice and in a second independent *Flicr* KO mouse. (*A*) *Flicr* deletion is not in a region containing epigenetic marks of enhancers (H3K27Ac), active promoters (H3K4me3), suppressive marks (H3K27me3) in Tregs or Tconvs, and CpG islands. (*B*) Proportion of FoxP3$^+$ Tregs among CD4$^+$TCRβ^+ T cells in different organs in *Flicr* WT and KO mice. Data are pooled from four experiments; each dot represents one mouse. (Bottom) Representative FACS plot. (*C*) Effect of *Flicr* on FoxP3 expression in vivo is also observed in B6xNOD mice. FoxP3 vs. CD25 protein expression in gated CD4$^+$ T cells from *Flicr* WT and KO B6xNOD mice. (*Left*) Representative plot. (*Right*) Compiled FoxP3 MFI and proportion of FoxP3^{lo} cells (per gating at left). Each dot represents one mouse; dashed lines connect littermates. (*D*) Effect of *Flicr* on FoxP3 expression in vivo is also observed in another independent mutant with a 12-bp deletion of the donor splice site of exon 3 (Fig. 3*A*). Shown is FoxP3 vs. CD25 protein expression in gated CD4$^+$ T cells from in *Flicr* WT and KO in the spleen and lymph nodes. (*Left*) FACS plots. (*Right*) Compiled FoxP3 MFI and proportion of FoxP3^{lo} cells (per gating at left) in thymus, spleen, and lymph nodes.

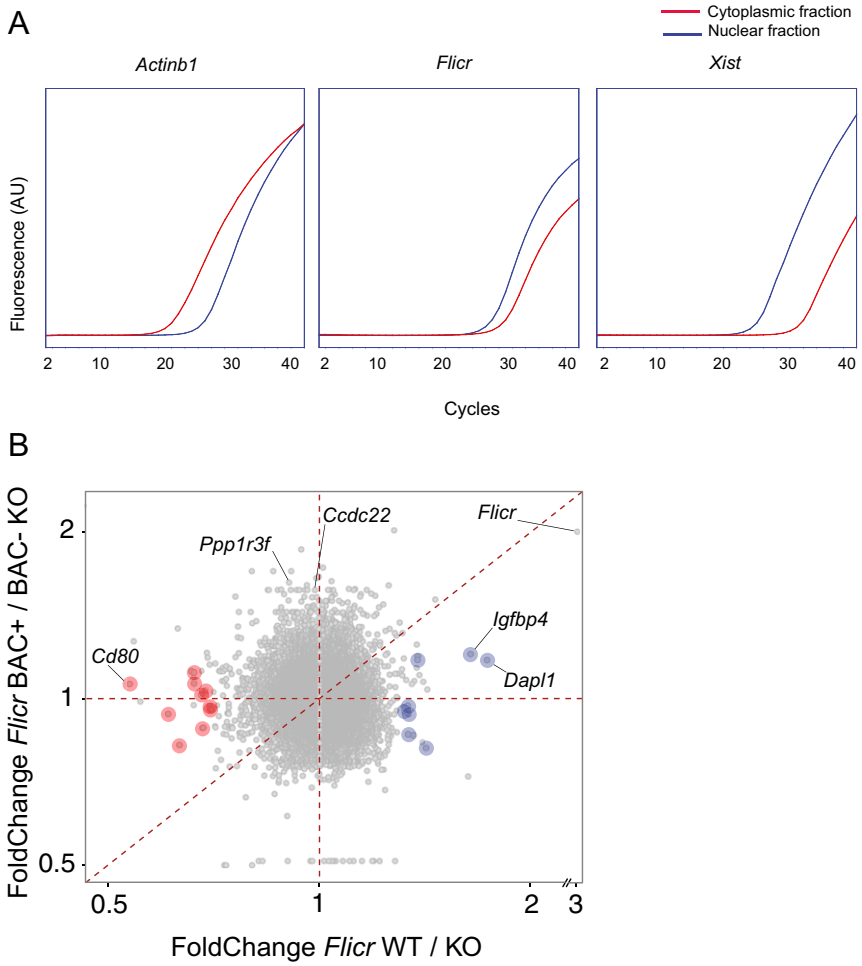

Fig. S4. *Flicr* is a *cis*-acting nuclear RNA. (*A*) *Flicr* is enriched in the nuclear fraction. Nucleocytoplasmic separation of splenic $CD4^+$ cells was performed by treatment with a hypotonic lysis buffer and centrifugation. *Flicr*, *Xist* (nuclear RNA), and *Actinß1* (cytoplasmic RNA) were amplified by RT-qPCR. Representative amplification curves for *Actinß1*, *Flicr*, and Xist from the nuclear (blue) or cytoplasmic (red) fractions are shown. (*B*) *Flicr* transgenic expression does not complement the gene expression differences induced by the absence of *Flicr*. The plot represents the gene expression fold change between *Flicr*-WT and KO Tregs on the *x*-axis vs. the gene expression fold change between BAC transgenic and nontransgenic KO Tregs on the *y*-axis. Blue and red genes are *Flicr*-induced and repressed genes, respectively, as gated in Fig. 5*A*.